Structure and related properties of amorphous magnesium aluminosilicates

Lawrence V. D. Gammond ,[1] Rita Mendes Da Silva ,[1] Anita Zeidler ,[1] Hesameddin Mohammadi ,[1]
Randall E. Youngman ,[2] Bruce G. Aitken,[2] Pierre Florian ,[3] Daniel R. Neuville ,[4] Louis Hennet ,[5] Henry E. Fischer ,[6]
Alex C. Hannon ,[7] Chris J. Benmore ,[8] and Philip S. Salmon [1,*]

[1]*Department of Physics, University of Bath, Bath, BA2 7AY, United Kingdom*
[2]*Science and Technology Division, Corning Incorporated, Corning, New York 14831, USA*
[3]*CNRS, Conditions Extrêmes et Matériaux: Haute Température et Irradiation (CEMHTI) UPR 3079, Université d'Orléans, Orléans, France*
[4]*Université de Paris, Institut de physique du globe de Paris, CNRS-UMR 7154, Paris 75005, France*
[5]*Interfaces, Confinement, Matériaux et Nanostructures, UMR7374, CNRS, Université d'Orléans, 45071 Orléans Cedex 2, France*
[6]*Institut Laue Langevin, 71 Avenue des Martyrs, 38042 Grenoble Cedex 9, France*
[7]*ISIS Facility, Rutherford Appleton Laboratory, Chilton, Didcot, Oxon OX11 0QX, United Kingdom*
[8]*X-ray Science Division, Advanced Photon Source, Argonne National Laboratory, 9700 South Cass Avenue, Lemont, Illinois 60439, USA*

The structure of the magnesium aluminosilicate glasses $(MgO)_x(Al_2O_3)_y(SiO_2)_{1-x-y}$, where $0 \leqslant x < 1$, $0 \leqslant y < 1$ and $x + y < 1$, was explored by neutron and x-ray diffraction, aided by the results from ^{27}Al magic angle spinning nuclear magnetic resonance spectroscopy. A wide composition range was investigated, using aerodynamic levitation with laser heating to extend the glass-forming region well into the peraluminous regime where $R = x/y < 1$. The results were interpreted with the aid of an analytical model for the composition-dependent structure where magnesium ions do not contribute towards the glass network. The model delivers Al-O bond distances typical of fourfold and fivefold coordinated aluminum atoms. It also delivers Mg-O coordination numbers of 4.46(9) and 5.39(10) for magnesium in a predominantly network-modifying versus charge-compensating role, corresponding to Mg-O bond distances of 2.024(10) and 2.120(20) Å, respectively. The more compact coordination environment of the network modifier is related to an enhanced probability of magnesium finding nonbridging oxygen (NBO) atoms as the nearest neighbors. Structural change is observed along the tectosilicate tie line in the transformation from a "normal" to "anomalous" glass, where the mechanism of deformation under sharp-contact loading changes from shear flow to densification. A minimum in the composition dependence of the glass hardness is related to a minimum in the Al-O coordination number and to a competition between the availability of NBO atoms, which break the connectivity of the tetrahedral network, versus high cation field-strength Mg^{2+} and fivefold and sixfold coordinated Al^{3+} ions, which cross-link the pieces of the network thus fragmented.

I. INTRODUCTION

Magnesium is a critical component in amorphous aluminosilicates that have widespread applications ranging from commercial display glass [1] to the models for magmatic materials in geoscience [2,3].

In active matrix displays, Si-based devices are deposited onto a flat glass substrate, and alkaline earth oxides are employed in the glass-making process in order to avoid high-mobility alkali ions that can migrate from the glass structure to poison these devices [1]. Here, alkaline earths like MgO are used to decrease the liquidus temperature and promote a large liquidus viscosity, which is necessary for making flat glass

sheets via the fusion-draw process, whilst helping to suppress crystallization. As compared to its alkaline earth counterparts, an MgO containing glass will (i) have a higher strain point, which is important for accessing the high-temperature processing conditions where Si-based devices are deposited; (ii) be less dense, which is beneficial for making lighter weight products; (iii) have a smaller coefficient of thermal expansion, which can be used to advantage when matching the coefficient of the glass substrate to silicon in order to minimize thermal stress; and (iv) have a larger Young's modulus, which leads to stiffer glass that will exhibit less elastic distortion. MgO is also used to tune the compressive stress in display glass that is strengthened by ion exchange [4]. Its addition to Al_2O_3–SiO_2 improves the crack resistance, which can be adjusted, along with the hardness, by varying the glass composition [5].

MgO is a key component in the $CaO-MgO-Al_2O_3-SiO_2$ (CMAS) family of crustal and mantle minerals [2], where the glass under pressure is often used as a model system for dry basaltic melts [6,7]. Ingested materials from the CMAS family have a deleterious effect on the operation of gas-turbine engines when they melt and react with the thermal

---

*Corresponding author: p.s.salmon@bath.ac.uk

barrier coatings of components in the hot sections of those engines [8–10]. Glass ceramics from the CMAS system find applications that range from the cordierite substrates used for catalytic converters in the automobile industry [11], to the sealant for solid oxide fuel cells [12]. Magnesium aluminosilicate (MgAS) glasses are possible supplementary cementitious materials, which contribute towards the properties of hardened concrete [13].

In all these applications, the structural role of magnesium in the vitreous state is largely unknown. This situation arises from (i) the chameleon-like nature of magnesium, which has the ability to take an Mg-O coordination number from 4 to 6 or beyond, and (ii) the lack of definitive structural information from experiment. For instance, information from ^{25}Mg magic angle spinning (MAS) nuclear magnetic resonance (NMR) experiments is scarce because of the low natural abundance (10%), low gyromagnetic ratio, and significant quadrupole moment (nuclear spin $I = 5/2$) of the ^{25}Mg isotope [14].

We have therefore been motivated to explore the structure of the MgAS glasses $(MgO)_x(Al_2O_3)_y(SiO_2)_{1-x-y}$, where $0 \leqslant x < 1$, $0 \leqslant y < 1$ and $x + y < 1$, by neutron diffraction (ND) and x-ray diffraction (XRD). In this work, the aluminum speciation obtained from ^{27}Al MAS NMR experiments is used as a constraint in the interpretation of the measured pair-distribution functions. In general, the diffraction and ^{27}Al MAS NMR experiments were performed on the same sample of a given glass. A wide range of compositions was investigated along tie lines in the ternary composition diagram where the silica content was kept constant at 50, 60, or 70 mol%, using aerodynamic levitation with laser heating (i.e., containerless processing) to extend the glass-forming region well into the peraluminous regime where the ratio $R = x/y < 1$. The tectosilicate tie line was also investigated where $R = 1$. Along this join, the charge on Mg^{2+} can be balanced by forming two $[AlØ_{4/2}]^-$ units, where Ø denotes a bridging oxygen (BO) atom, which gives the possibility of a network in which all the silicon atoms are in $SiØ_{4/2}$ units, i.e., the number of nonbridging oxygen (NBO) atoms per tetrahedron $N_{NBO}/N_T = 0$. The results are interpreted with the aid of a recently developed analytical model for the composition-dependent structure of aluminosilicate glasses, which will be referred to as the GYZAS model following the first letters of the surnames of its authors [15].

This paper is organized as follows. The essential diffraction theory is given in Sec. II. The sample preparation, ^{27}Al MAS NMR and diffraction experiments are described in Sec. III and the results are summarized in Sec. IV. The GYZAS model for MgAS glasses is outlined in Sec. V and is used in Sec. VI to help interpret the diffraction results. The effect of the structure on the glass hardness is also considered. Conclusions are drawn in Sec. VII.

II. THEORY

The total structure factor measured in a diffraction experiment is given by [21]

$$S(k) = 1 + \frac{1}{\langle w(k) \rangle^2} \sum_\alpha \sum_\beta c_\alpha c_\beta w_\alpha(k) w_\beta(k) [S_{\alpha\beta}(k) - 1], \quad (1)$$

where k is the magnitude of the scattering vector; c_α is the atomic fraction of chemical species α; $w_\alpha(k)$ is the k-dependent x-ray atomic form-factor $f_\alpha(k)$ or the k-independent coherent neutron scattering length b_α of chemical species α; the mean value $\langle w(k) \rangle = \sum_\alpha c_\alpha w_\alpha(k)$; and $S_{\alpha\beta}(k)$ is the Faber-Ziman partial structure factor for the chemical species α and β. Neutral atom form-factors were used in the XRD data analysis [22]. The neutron scattering lengths of the elements are $b_{Mg} = 5.375(4)$ fm, $b_{Al} = 3.449(5)$ fm, $b_{Si} = 4.1491(10)$ fm, and $b_O = 5.803(4)$ fm [23].

The total pair-distribution function is given by the Fourier transform relation

$$D'(r) = \frac{2}{\pi} \int_0^\infty dk\, k[S(k) - 1]M(k)\sin(kr)$$
$$= D(r) \otimes M(r), \quad (2)$$

where r is a distance in real space and $\otimes$ is the one-dimensional convolution operator. $M(k)$ is a window function given by $M(k) = 1$ for $k \leqslant k_{max}$ and $M(k) = 0$ for $k > k_{max}$, where k_{max} is the maximum accessible k value, and $M(r)$ is the real-space manifestation of $M(k)$. In the case when k_{max} is sufficiently large that $M(k)$ does not truncate the oscillations in $S(k)$, Eq. (2) delivers the unmodified total pair-distribution function $D(r)$.

In an ND experiment

$$D(r) = \frac{4\pi \rho r}{\langle b \rangle^2} \sum_\alpha \sum_\beta c_\alpha c_\beta b_\alpha b_\beta [g_{\alpha\beta}(r) - 1], \quad (3)$$

where ρ is the atomic number density, $\langle b \rangle$ is the mean neutron coherent scattering length, and $g_{\alpha\beta}(r)$ is the partial pair-distribution function for the chemical species α and β. Each peak i in $rg_{\alpha\beta}(r)$ was represented by the Gaussian function

$$p_{\alpha\beta}^i(r) = \frac{1}{4\pi \rho} \frac{\bar{n}_\alpha^\beta(i)}{c_\beta^i r_{\alpha\beta}^i} \frac{1}{\sqrt{2\pi}\sigma_{\alpha\beta}^i} \exp\left[-\frac{(r - r_{\alpha\beta}^i)^2}{2(\sigma_{\alpha\beta}^i)^2}\right], \quad (4)$$

where $r_{\alpha\beta}^i$, $\sigma_{\alpha\beta}^i$, and $\bar{n}_\alpha^\beta(i)$ are the peak position, standard deviation and coordination number of chemical species β around α, respectively. The measured $D'(r)$ function was fitted to a sum of these Gaussian peaks, convoluted with $M(r)$, using the procedure described in Ref. [24]. The goodness of fit was assessed by the parameter R_χ [25].

In the XRD experiments, the contribution of each Gaussian peak $p_{\alpha\beta}^i(r)$ to $S(k) - 1$ was calculated and Fourier transformed to real-space using the same $M(k)$ function as used for the experimental data [24]. A least squares procedure was then used to fit an appropriate sum of these Fourier transforms to $T'(r) = T(r) \otimes M(r)$ using the program PXFIT (A. C. Hannon, private communication), where $T(r) \equiv D(r) + T^0(r)$ and $T^0(r) = 4\pi \rho r$. The fitted functions are presented as $D'(r) = [T(r) - T^0(r)] \otimes M(r) = T'(r) - 4\pi \rho r$ for ease of comparison with the neutron diffraction results.

In the following, the functions measured by neutron and x-ray diffraction will be denoted by the subscripts "N" and "X," respectively.
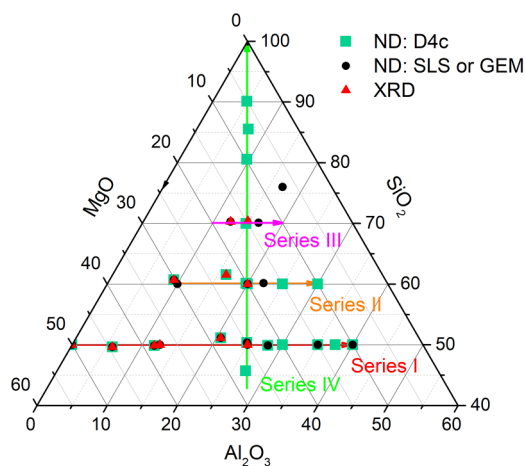
FIG. 1. Ternary diagram showing the glass compositions investigated by using ND with the instrument D4c, SLS or GEM, or by using XRD. Series I–III correspond to tie lines with 50, 60, and 70 mol% silica, respectively, and series IV corresponds to the tectosilicate tie line.

III. EXPERIMENT

A. Sample preparation and characterization

The compositions of the investigated MgAS glasses are shown in Fig. 1. The glasses were prepared by using either a classic bulk-quenching procedure or containerless processing, and are designated by MgAS_x_$(100 - x - y)$, with x and y expressed in mol%.

The first set of glasses was made by melting 900–1000 g batches in covered Pt or Pt/Rh crucibles at 1650 °C, and pouring the melt onto a steel table. In some cases, the material was double melted to ensure glass homogeneity. The glasses were annealed at a temperature in the range 700 °C–750 °C [15,16].

The second set of glasses was made by first mixing ∼100 g batches of an appropriate quantity of MgO, Al_2O_3 and SiO_2 powders (Rectapur, Merck) under alcohol in an agate mortar for 1 h [17]. Each mixture was dried by slowly heating to 1000 °C. The glass was prepared by melting the mixture in a covered platinum alloy crucible at 1627 °C, equilibrating for between 4 and 6 h, and dipping the bottom of the crucible into distilled water. The sample was then crushed, remelted and requenched four times to ensure glass homogeneity.

The third set of glasses was prepared from high purity MgO (Aldrich, 99.999%), Al_2O_3 (Sigma-Aldrich, 99.998%) and SiO_2 (Alfa Aesar, 99.9%) powders that had been calcined at 1000 °C [18]. For each sample, a batch of powder of mass ∼2–3 g was melted in a Pt/10%Rh crucible at 1550 °C or 1650 °C for 1 h, and the melt was quenched by placing the bottom of the crucible onto a liquid-nitrogen cooled copper block. In some cases, the material was double melted to ensure glass homogeneity. The MgAS_50_50_a glass of mass ∼3 g was made by calcining powdered MgO (Alfa Aesar, ≥99.995%) and SiO_2 (Alfa Aesar, 99.9%) at 1000 °C, mixing the powders by shaking, and melting the mixture in a Pt/10%Rh crucible at 1650 °C for 2 h. The melt was quenched by placing the bottom of the crucible in water. The sample was ground, and the melt and quench procedure was then repeated. The overall

mass loss during processing was ∼1%, which was probably related to the loss of re-adsorbed water.

The fourth set of glasses corresponds to compositions with ⩾80 mol% silica. Each glass was made by a double melting procedure, employing iridium crucibles in an induction furnace at 2000 °C, and was annealed at 800 °C [16]. The glasses did not show any visible phase separation.

The final set of glasses corresponds to compositions with a high alumina content in the peraluminous regime [17]. The starting ceramic or glass-ceramic material was made in the same way as the second set of glasses but with a melt temperature of 1677 °C–1727 °C. The material was melted in an aerodynamic levitation device using a CO_2 laser and an argon/oxygen mixture (21% oxygen by volume) as the flow gas (CEMHTI, Orléans). The glass was formed by switching the laser power off.

The composition of each glass was measured using either inductively coupled plasma - optical emission spectrometry [15,16] or electron microprobe analysis [17], or it was taken from the batch composition. The density was measured using a helium pycnometer. The glass compositions and densities are summarized in Table I. The aluminum speciation for the majority of the glass samples is reported elsewhere [15–17].

B. Solid-state NMR experiments

For several newly prepared glasses along the 60 mol% silica tie line, ^{27}Al MAS NMR experiments were performed using a Bruker Avance III spectrometer working with a principal magnetic field of 20.0 T ([27]Al Larmor frequency of 221.5 MHz). The powdered samples were spun at 33.3 kHz in 2.5 mm diameter zirconia rotors. To retrieve quantitative spectra, a pulse of 0.5 μs with a radio-frequency field strength of 50 kHz was used, giving a flip angle of less than $\pi/18$ as measured for the reference solution [26]. This short pulse leads to a broad excitation of the spinning sideband manifold, which is acquired over a large 2.5 MHz spectral width, the rolling baseline induced by the 4.8 μs dead time being removed in an automated way [27]. Spin-lattice relaxation times were estimated at around 0.5 s and a recycle delay of 0.5 s was chosen accordingly, with 500 to 8000 transients accumulated depending on the alumina content of each sample. All spectra are referenced to a 1 M solution of $Al(NO_3)_3$ in HNO_3.

Spectra were simulated with a modified version of DMFit [28] assuming a statistical distribution of the local environments (the so-called GIM or "Czjzek" model [29]) leading to a set of four variable parameters per aluminum site: the population, mean isotropic chemical shift $\bar{\delta}_{iso}$, full width at half maximum of a Gaussian distribution of isotropic chemical shifts $\Delta\bar{\delta}_{iso}$, and standard deviation of a Gaussian distribution of quadrupolar interactions σ_c. Fits were made to the line shapes of both the central transition $\langle 1/2, -1/2 \rangle$ and the spinning sidebands generated by the external $\langle \pm 1/2, \pm 3/2 \rangle$ and $\langle \pm 3/2, \pm 5/2 \rangle$ transitions (when visible). The position and width of the latter provide additional experimental constraints on the fit. One should note that with the current acquisition conditions the spinning sidebands have significant intensities and their so-called "$n = 0$" component lies below the center line. It is therefore necessary to account for this additional intensity if one wants to retrieve precise site populations.

TABLE I. MgAS glass compositions and characterization. The glasses were prepared by classic bulk-quenching (BQ) or containerless processing (CP). The number density ρ is given with an error of ± 0.0001 Å^{-3}. The ND work used the instrument SLS, GEM, or D4c, and the XRD work used beamline 6-ID-D. The speciation found from the ^{27}Al MAS NMR experiments is given (with an error of ± 1–2%) along with the mean Al-O coordination number $\bar{n}_{\mathrm{Al}}^{\mathrm{O}}$. The latter was calculated using the full precision of the values found for the speciation from the NMR analysis.

Glass	x	y	$1-x-y$	R	Method	ρ (Å^{-3})	Diffraction method	Al(IV) (%)	Al(V) (%)	Al(VI) (%)	$\bar{n}_{\mathrm{Al}}^{\mathrm{O}}$	^{27}Al NMR reference
MgAS_27_46	0.2742	0.2689	0.4569	1.020	BQ[a]	0.0810	SLS	86	13	1	4.15(5)	[16]
MgAS_50_50_a	0.5000	–	0.5000	–	BQ[b]	0.0819	GEM, XRD	–	–	–	–	–
MgAS_50_50_b	0.4962	–	0.5038	–	BQ[c]	0.0806	D4c[f]	–	–	–	–	–
MgAS_44_50	0.4443	0.0592	0.4965	7.505	BQ[d]	0.0818	SLS, D4c, XRD	91	9	0	4.09(5)	[15]
MgAS_38_50	0.3837	0.1177	0.4987	3.260	BQ[d]	0.0810	SLS, D4c, XRD	91	9	0	4.09(5)	[15]
MgAS_37p5_50	0.3750	0.1250	0.5000	3.000	BQ[b]	0.0804	D4c, XRD	–	–	–	4.09[g]	[15]
MgAS_28_51	0.2825	0.2062	0.5113	1.370	BQ[d]	0.0792	SLS, D4c, XRD	88	12	0	4.12(5)	[15]
MgAS_25_50_a	0.2490	0.2476	0.5034	1.006	BQ[a]	0.0797	SLS, D4c	87	12	1	4.13(5)	[16]
MgAS_25_50_b	0.2500	0.2500	0.5000	1.000	BQ[b]	0.0795	D4c, XRD	–	–	–	4.13[g]	[16]
MgAS_22_50	0.2216	0.2794	0.4990	0.793	BQ[d]	0.0799	SLS, D4c	80	19	1	4.21(5)	[15]
MgAS_20_50	0.2000	0.3000	0.5000	0.667	CP[e]	0.0798	SLS	70	25	5	4.36(5)	[17]
MgAS_15_50	0.1500	0.3500	0.5000	0.429	CP[e]	0.0804	SLS, D4c	63	32	5	4.42(5)	[17]
MgAS_13_50	0.1250	0.3750	0.5000	0.333	CP[e]	0.0798	SLS	–	–	–	4.54[g]	[17]
MgAS_10_50	0.1000	0.4000	0.5000	0.250	CP[e]	0.0809	SLS, D4c	46	42	12	4.66(5)	[17]
MgAS_30_61	0.3015	0.0918	0.6067	3.284	BQ[d]	0.0773	SLS, D4c, XRD	94	6	0	4.06(5)	[15]
MgAS_30_60_a	0.3000	0.1000	0.6000	3.000	BQ[e]	–	–	94	5	1	4.06(2)	This work
MgAS_30_60_b	0.3000	0.1000	0.6000	3.000	BQ[b]	0.0771	D4c	–	–	–	4.06[g]	[15]
MgAS_24_60	0.2400	0.1600	0.6000	1.500	BQ[e]	–	–	94	6	0	4.07(1)	This work
MgAS_22_62	0.2227	0.1619	0.6154	1.376	BQ[d]	0.0767	SLS, XRD	86	13	1	4.15(5)	[15]
MgAS_19p7_60	0.2016	0.1973	0.6011	1.022	BQ[a]	0.0771	SLS	90	10	0	4.11(5)	[16]
MgAS_20_60_a	0.2000	0.2000	0.6000	1.000	BQ[e]	0.0771	SLS	90	10	0	4.11(2)	This work
MgAS_20_60_b	0.2000	0.2000	0.6000	1.000	BQ[b]	0.0766	D4c, XRD	–	–	–	4.11[g]	[16]
MgAS_18_60	0.1763	0.2222	0.6015	0.793	BQ[d]	0.0772	D4c	78	19	3	4.25(5)	[15]
MgAS_15_60	0.1500	0.2500	0.6000	0.600	BQ[e]	0.0767	SLS	82	17	1	4.20(3)	This work
MgAS_10_60	0.1000	0.3000	0.6000	0.333	CP[e]	0.0750	SLS	71	26	3	4.32(3)	This work
MgAS_17_70	0.1728	0.1244	0.7028	1.389	BQ[d]	0.0737	D4c, XRD	82	16	2	4.20(5)	[15]
MgAS_15_70_a	0.1522	0.1481	0.6997	1.028	BQ[a]	0.0737	SLS	90	9	1	4.11(5)	[16]
MgAS_15_70_b	0.1476	0.1484	0.7040	0.995	BQ[d]	0.0736	XRD	78	19	3	4.25(5)	[15]
MgAS_13_70	0.1336	0.1654	0.7010	0.808	BQ[d]	0.0741	D4c	74	22	4	4.30(5)	[15]
MgAS_7_76	0.0700	0.1700	0.7600	0.412	BQ[e]	0.0735	D4c	94	6	0	4.06(5)	[17]
MgAS_10_81	0.0982	0.0962	0.8056	1.021	BQ[a]	0.0708	SLS	90	9	1	4.11(5)	[16]
MgAS_7_86	0.0709	0.0738	0.8553	0.961	BQ[a]	0.0701	SLS	87	11	2	4.14(5)	[16]
MgAS_5_90	0.0501	0.0487	0.9012	1.029	BQ[a]	0.0698	SLS	87	11	2	4.14(5)	[16]
MgAS_0_100	0.0000	0.0000	1.0000	–	BQ	0.0662	D4c[h]	–	–	–	–	–

The sample preparation is described in more detail in [a]Ref. [16]; [b]Ref. [18]; [c] Ref. [19]; [d]Ref. [15]; or [e]Ref. [17]. [f]ND data taken from Ref. [19]; [g]Estimated; [h]ND data taken from Ref. [20].

When the intensity of a given site appeared to be below a few percent, $\Delta\bar{\delta}_{\mathrm{iso}}$ and σ_{c} were kept fixed during the fitting routine.

C. Diffraction experiments

The ND work used the instruments SANDALS (SLS) [30] and GEM [31] at the ISIS pulsed neutron source and the instrument D4c at the Institut Laue-Langevin [32].

In the SLS experiments, the quasispherical samples made by containerless processing were held in a cylindrical vanadium container of inner diameter 5.00 mm and wall thickness 0.04 mm. The other samples were coarsely ground and held in a cylindrical vanadium container of inner diameter 10.30 mm and wall thickness 0.04 mm. Diffraction patterns were measured at room temperature ($\simeq$298 K) for each of the samples in its container, an empty container of each size, the empty

instrument, and a cylindrical rod of the null-scattering alloy $V_{0.9486}Nb_{0.0514}$ (diameter 7.95 mm) for normalization purposes. The data sets were processed using the GUDRUN analysis program [33] with inelasticity corrections calculated according to Ref. [34]. The GEM experiment proceeded similarly, with the sample held in a cylindrical vanadium container of inner diameter 5.00 mm and wall thickness 0.04 mm.

In the D4c experiments, the samples made by containerless processing were held in a cylindrical vanadium container of inner diameter 4.8 mm and wall thickness 0.1 mm. The other samples were coarsely ground and held in a cylindrical vanadium container of inner diameter 6.8 mm and wall thickness 0.1 mm. The incident wavelength was 0.4980(1) Å. Diffraction patterns were measured at room temperature ($\simeq$298 K) for each of the samples in its container, an empty container of each size, the empty instrument, and
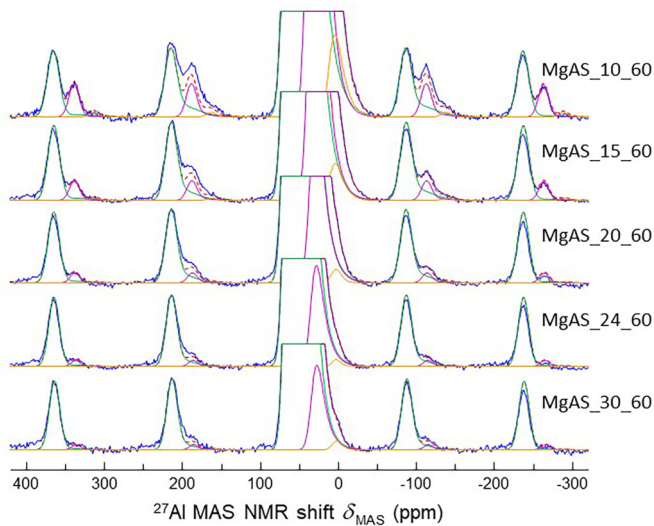
FIG. 2. Line shapes of the central transition and spinning side-bands in the measured ^{27}Al MAS NMR spectra for several of the MgAS glasses (blue curves). The Czjzek fit to the spectral components is given by the green curve for Al(IV), the magenta curve for Al(V), and the orange curve for Al(VI). The sum of the fitted functions is given by the broken red curve, which overlays the blue curve at most values of δ_{MAS}. The central peak, which is truncated for clarity of presentation, is shown in full in Fig. 3.

FIG. 3. Line shape of the central transition in the measured ^{27}Al MAS NMR spectra for the MgAS glasses shown in Fig. 2 (blue curves). The Czjzek fit is given by the green curve for Al(IV), the magenta curve for Al(V), and the orange curve for Al(VI). The sum of the fitted functions is given by the broken red curve, which overlays the blue curve at most values of δ_{MAS}.

a cylindrical vanadium rod of diameter 6.08 or 6.37 mm for normalization purposes. The data analysis followed the procedure described in Ref. [35].

Two different XRD experiments were performed using beamline 6-ID-D at the Advanced Photon Source with a Varex 4343CT amorphous silicon flat panel detector. The incident photon energy was either 100.334 or 100.233 keV, corresponding to experiments with a sample to detector distance of either 281 or 311 mm, respectively, as found from the diffraction pattern measured for crystalline CeO$_2$. Cylindrical Kapton polyimide tubes of 1.80(1) mm internal diameter and 0.051(6) mm wall thickness were used to hold the powdered glass samples. Diffraction patterns were measured for each sample in its container, an empty container and the empty instrument. The data were converted to one-dimensional diffraction patterns using FIT2D [36] and the corrections for background scattering, beam polarization, attenuation, and Compton scattering were made using PDFgetX2 [37].

IV. RESULTS

A. Aluminum speciation

The Czjzek fits to the line shapes of both the central transition and spinning sidebands are shown in Figs. 2 and 3 for the 60 mol% silica glasses. The fitted parameters are listed in Table S1 [38] where the errors are those estimated by the fitting routine and reported by DMFit. The results show that, as the alumina content increases, the fraction of fourfold coordinated aluminum Al(IV) decreases and the fraction of higher coordinated aluminum increases, consistent with previous findings [15–17,39,40]. For comparison, Table S2 [38] lists the parameters obtained from Czjzek fits to the line shape
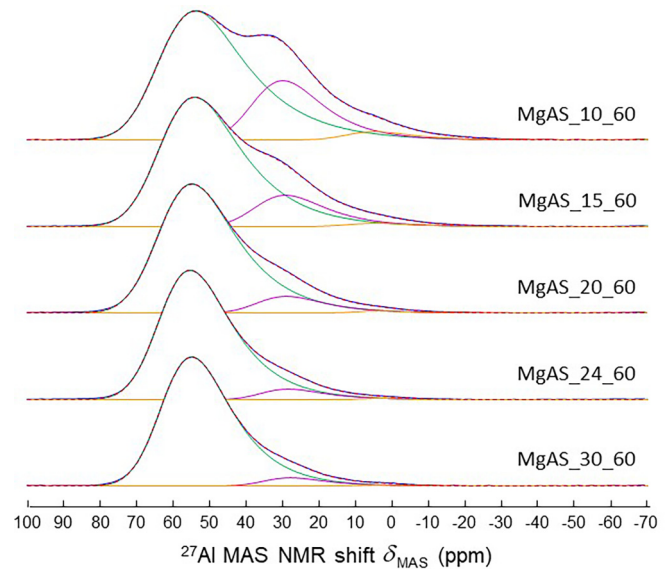
of just the central transition. For a given glass composition, the more accurate fit to both the central peak and spinning sidebands shows less Al(IV) and more fivefold coordinated aluminum Al(V) and sixfold coordinated aluminum Al(VI).

Table I lists the aluminum speciation and Al-O coordination numbers found from all the solid-state NMR experiments. The results show that Al(IV) is in the majority for all compositions and that Al(V) is the second most abundant species. In the regime where $R \geqslant 1$, Al(VI) occurs rarely ($\leqslant 2\%$) or is absent. In the peraluminous regime, the proportion of Al(IV) species decreases with R along both the 50 and 60 mol% silica tie lines.

B. Diffraction results

The neutron and x-ray total structure factors for the glasses with 50 mol% silica are shown in Figs. 4 and 5, respectively. For a given composition, there is contrast between the neutron and x-ray results, which reflects the different sensitivity of these techniques to the various pair-correlation functions. As the MgO content of the glass decreases, there is a sharpening of the peak at $k \simeq 2.75$ Å^{-1} in the $S_N(k)$ functions. Systematic changes to these functions are also observed as the silica content increases along the tectosilicate tie line (Fig. 6). The total structure factors for the other glasses are shown in Figs. S1–S3 [38].

The fitted $D'_N(r)$ functions for the glasses with 50 mol% silica are shown in Fig. 7 and in Figs. S4–S6 [38]. The fitted $D'_X(r)$ functions for this tie line are shown in Fig. 8. The fitted $D'_N(r)$ functions are illustrated in Figs. S7–S8 [38] for the glasses with 60 mol% silica and in Fig. S9 [38] for the MgAS_7_76 glass and the glasses with 70 mol% silica. The fitted $D'_X(r)$ functions for the glasses with either 60 or 70
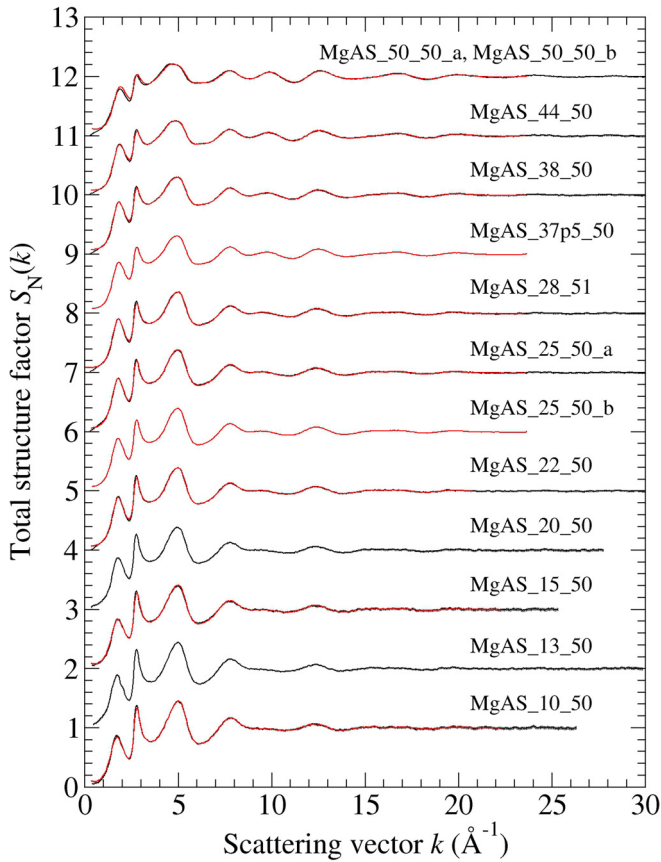
FIG. 4. The $S_N(k)$ functions for the MgAS glasses with 50 mol% silica measured using SLS/GEM (black curves) or D4c (red curves). The vertical error bars are smaller than the curve thickness at most k values. For clarity of presentation, several of the curves are displaced vertically and the data sets are shown to 30 Å^{-1}.

FIG. 5. The $S_X(k)$ functions for the MgAS glasses with 50 mol% silica. Several of the curves are displaced vertically for clarity of presentation.

mol% silica are shown in Fig. S10 [38]. Lastly, the fitted $D'_N(r)$ functions for the tectosilicate tie line are illustrated in Fig. 9 and in Fig. S11 [38].
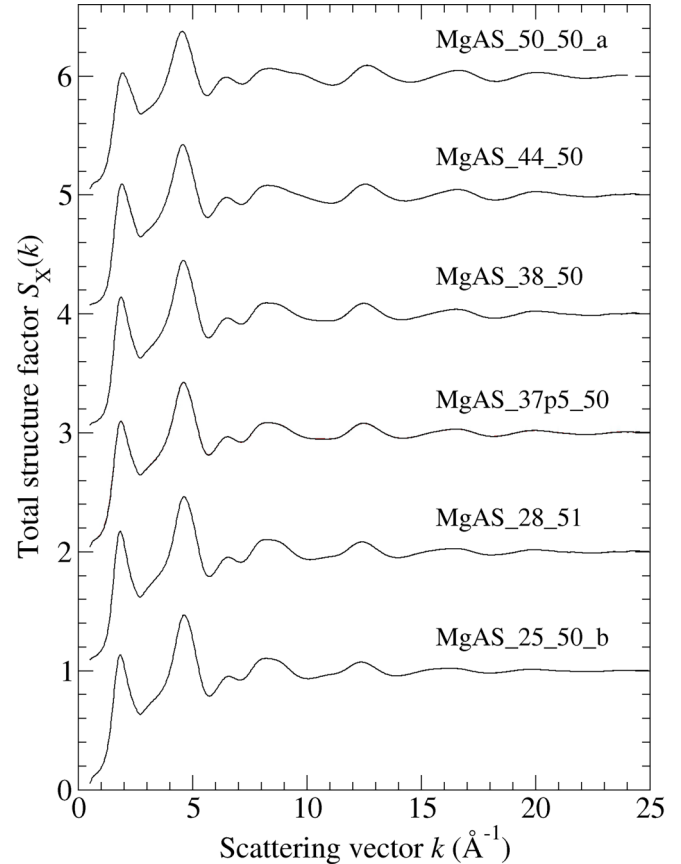
In the fitting procedure, the peaks in $D'(r)$ were assigned by reference to the Si-O, Al-O, Mg-O and O-O coordination environments observed for the crystalline phases (Table II). The Si-O coordination number was fixed at four, and the Al-O coordination number was fixed at the value

TABLE II. The Si-O, Al-O and Mg-O coordination numbers and bond distances for several Mg-containing crystalline systems.

| Crystal	x	y	$1-x-y$	R	Polyhedron	Atom pair	Distance (Å)	Reference
MgO	1.0000	0.0000	0.0000	–	MgO$_6$	Mg-O	2.109(1)	[41]
MgSiO$_3$	0.5000	0.0000	0.5000	–	SiO$_4$	Si-O	1.63(4)	[42]
					MgO$_6$	Mg-O	2.11(13)	
β-Mg$_2$SiO$_4$	0.6667	0.0000	0.3333	–	SiO$_4$	Si-O	1.64(9)	[43]
					MgO$_6$	Mg-O	2.09(9)	
Ca$_2$MgSi$_2$O$_7$	0.6000[a]	0.0000	0.4000	–	SiO$_4$	Si-O	1.624(26)	[44]
					MgO$_4$	Mg-O	1.916(5)	
Mg$_3$Al$_2$Si$_3$O$_{12}$	0.4286	0.1429	0.4286	3	SiO$_4$	Si-O	1.635(5)	[45]
					AlO$_6$	Al-O	1.887(5)	
					MgO$_8$	Mg-O	2.27(8)	
Mg$_{0.5}$AlSiO$_4$	0.2500	0.2500	0.5000	1	SiO$_4$	Si-O	1.66(5)	[46]
					AlO$_4$	Al-O	1.66(5)	
					MgO$_6$	Mg-O	2.31(38)	
MgAl$_2$O$_4$	0.5000	0.5000	0.0000	1	AlO$_6$	Al-O	1.928(2)	[47]
					MgO$_4$	Mg-O	1.923(1)	

[a]x gives the total MgO plus CaO content.
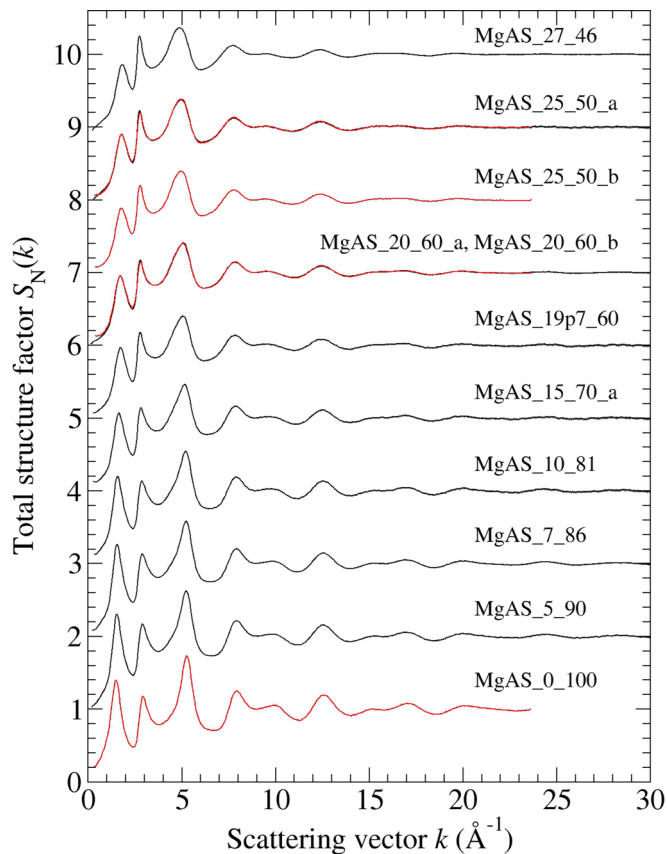
FIG. 6. The $S_N(k)$ functions for the MgAS glasses along the tectosilicate tie line measured using SLS (black curves) or D4c (red curves). The vertical error bars are smaller than the curve thickness at most k values. For clarity of presentation, several of the curves are displaced vertically and the data sets are shown to 30 Å^{-1}.

found from the ^{27}Al MAS NMR experiments (Table I). In all cases, the Mg-O peak is asymmetric, as found in experiments using the method of neutron diffraction with isotope substitution (NDIS) in which site specific information was gained on the magnesium coordination environment [18]. The Mg-O peak shape could be represented by the use of two (or occasionally three) Gaussian peaks. Table S3 [38] lists the k_{max} values used for $M(k)$ in the Fourier transformation of the measured $S(k)$ functions [Eq. (2)], the fitted r-space range in $D'(r)$, and the associated goodness-of-fit parameter R_χ. The fitted Si-O, Al-O and Mg-O peak parameters are listed in Tables S4–S8 [38].

For all the glasses with $\leqslant$70 mol% silica, the Mg-O coordination number is within the range $4 < \bar{n}_{Mg}^O < 6$. In comparison, the ^{25}Mg NMR spectra measured for a variety of molten magnesium aluminosilicates indicate that Mg^{2+} is between fivefold and sixfold coordinated in the melt, depending on the composition [48]. For the tectosilicate tie line, the fitted Mg-O coordination number exceeds six when the silica content $\gtrsim$80 mol%, but the contribution from the Mg-O correlations to $D'(r)$ is small, making it difficult to discern their contribution (Fig. 9 and Fig. S11 [38]). The change in structure along the tectosilicate tie line will be discussed in Sec. VI F.
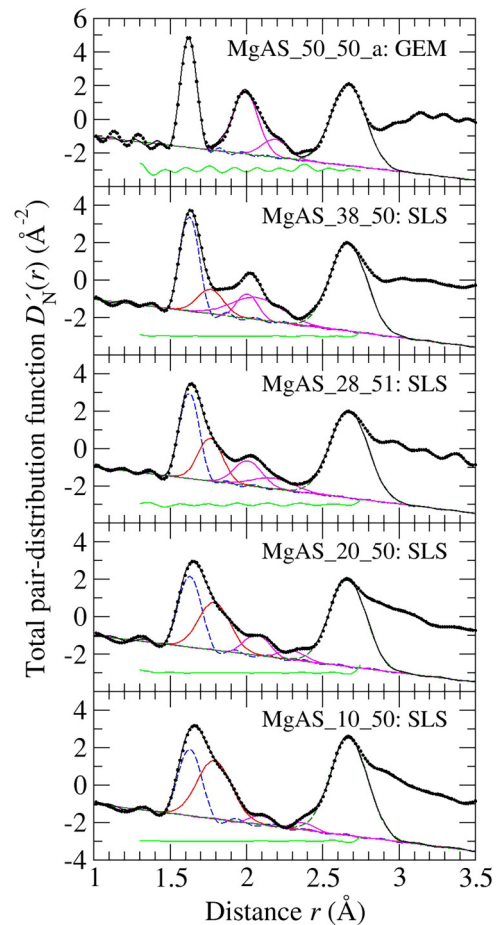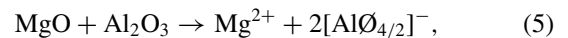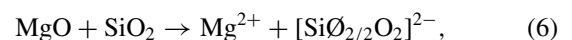

FIG. 7. The fitted $D'_N(r)$ functions for several of the MgAS glasses with 50 mol% silica. In a given panel, the filled circles give the measured function, the black solid curve gives the fitted function, and the other curves show the contributions from the Si-O (blue broken curve), Al-O (red solid curve), Mg-O (magenta solid curves), and O-O (green broken curve) correlations. The displaced green solid curve shows the residual. The O-O correlations were introduced to constrain the peaks fitted at smaller r values.

V. STRUCTURAL MODEL

The GYZAS [15] model for the structure of aluminosilicate glasses is based on a simple set of reactions in which the silicon atoms remain fourfold coordinated. For the case of the MgAS system, MgO reacts with Al$_2$O$_3$ according to a scheme such as

$$\text{MgO} + \text{Al}_2\text{O}_3 \rightarrow \text{Mg}^{2+} + 2[\text{AlØ}_{4/2}]^-, \qquad (5)$$

which generates network-forming Al(IV) atoms, or with SiO$_2$ according to a scheme such as

$$\text{MgO} + \text{SiO}_2 \rightarrow \text{Mg}^{2+} + [\text{SiØ}_{2/2}\text{O}_2]^{2-}, \qquad (6)$$

which generates NBO atoms as represented by the open oxygen symbol on the right-hand side. The Mg^{2+} ions in Eqs. (5) and (6) play charge-compensating versus network-modifying roles, respectively. Although they may adopt a fourfold coordination environment [49], as per the Si and Al(IV) atoms, they are not regarded as network formers (see Sec. VI H). The
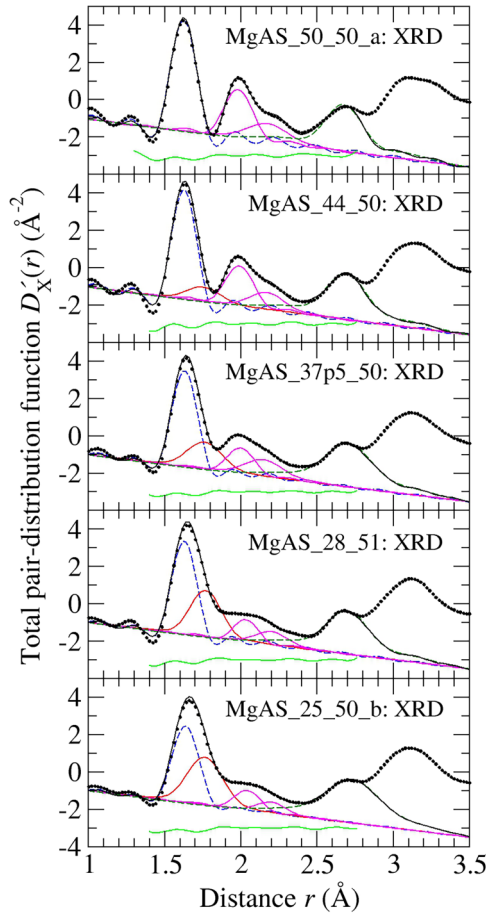
FIG. 8. The fitted $D'_X(r)$ functions for several of the MgAS glasses with 50 mol% silica. In a given panel, the filled circles give the measured function, the black solid curve gives the fitted function, and the other curves show the contributions from the Si-O (blue broken curve), Al-O (red solid curve), Mg-O (magenta solid curves), and O-O (green broken curve) correlations. The displaced green solid curve shows the residual. The O-O correlations were introduced to constrain the peaks fitted at smaller r values.
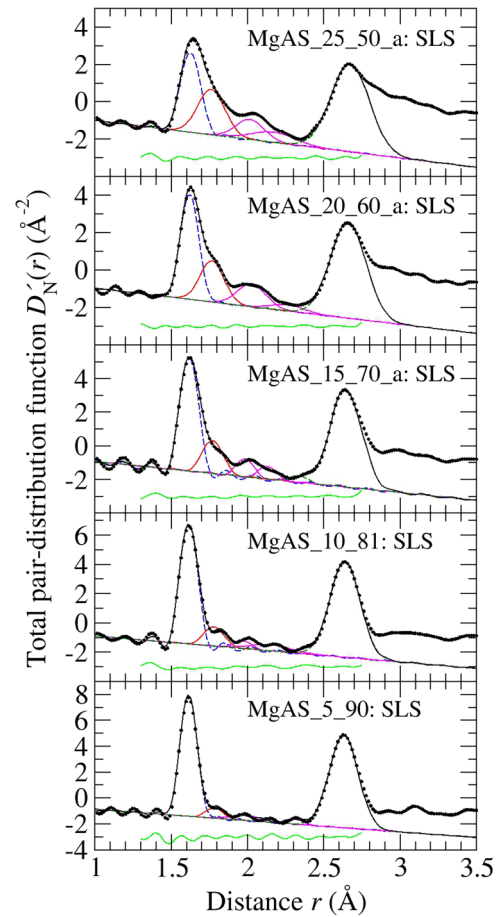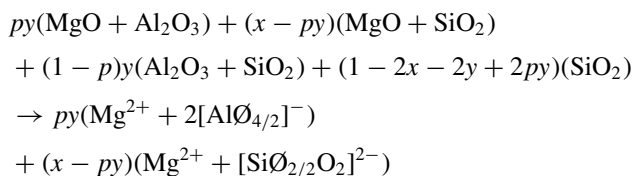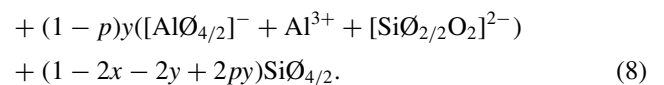
FIG. 9. The fitted $D'_N(r)$ functions for several of the MgAS glasses along the tectosilicate tie line. In a given panel, the filled circles give the measured function, the black solid curve gives the fitted function, and the other curves show the contributions from the Si-O (blue broken curve), Al-O (red solid curve), Mg-O (magenta solid curves), and O-O (green broken curve) correlations. The displaced green solid curve shows the residual. The O-O correlations were introduced to constrain the peaks fitted at smaller r values.

Al_2O_3 can also react with SiO_2 according to a scheme such as

$$Al_2O_3 + SiO_2 \rightarrow [Al\emptyset_{4/2}]^- + Al^{3+} + [Si\emptyset_{2/2}O_2]^{2-}, \quad (7)$$
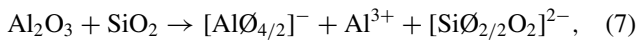
where the Al^{3+} ion serves the dual purpose of modifying the SiO_2 network by the creation of NBO atoms and compensating the charge on the $[Al\emptyset_{4/2}]^-$ unit. This modifying/charge-compensating aluminum species will be denoted by Al_{mcc}: it represents an Al(V) or Al(VI) atom, and is not treated as a network former.

On the magnesia-rich side of the ternary diagram where $R \geqslant 1$, it is convenient to write the glass composition as $[(MgO)(Al_2O_3)]_{py}[(MgO)(SiO_2)]_{x-py}[(Al_2O_3)(SiO_2)]_{(1-p)y}$ $(SiO_2)_{1-2x-2y+2py}$, where the parameter p is a constant $0 \leqslant p \leqslant 1$, and to consider the reaction scheme [15]

$$py(MgO + Al_2O_3) + (x - py)(MgO + SiO_2)$$

$$+ (1 - p)y(Al_2O_3 + SiO_2) + (1 - 2x - 2y + 2py)(SiO_2)$$

$$\rightarrow py(Mg^{2+} + 2[Al\emptyset_{4/2}]^-)$$

$$+ (x - py)(Mg^{2+} + [Si\emptyset_{2/2}O_2]^{2-})$$

$$+ (1 - p)y([Al\emptyset_{4/2}]^- + Al^{3+} + [Si\emptyset_{2/2}O_2]^{2-})$$

$$+ (1 - 2x - 2y + 2py)Si\emptyset_{4/2}. \quad (8)$$

Hence, the fraction of Al(IV) species is given by $f_{Al(IV)} = N_{Al(IV)}/N_{Al} = (1 + p)/2$, where $N_{Al(IV)}$ and N_{Al} are the number of Al(IV) aluminum atoms and total number of aluminum atoms, respectively. The relative importance of the reaction schemes in Eq. (8) is controlled by the value of p. For example, when $p = 1$ there is no reaction between Al_2O_3 and SiO_2, all the aluminum species are Al(IV), and these Al-centred tetrahedra are charge compensated by Mg^{2+} ions. The results are then consistent with the standard model for the structure of aluminosilicate glasses in which NBO atoms are absent at $R = 1$ [50]. However, when $p < 1$ it is possible to generate Al(V) and/or Al(VI) atoms, in accordance with the results found from the ^{27}Al MAS NMR experiments, such that NBO atoms are present at $R = 1$.

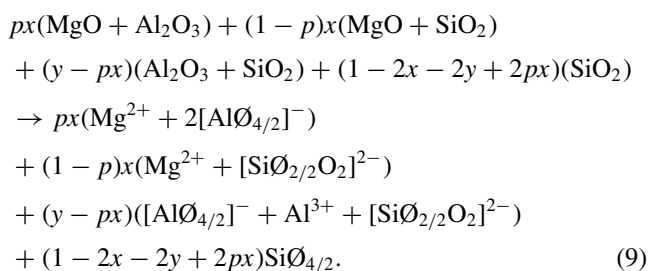On the Al_2O_3-rich or peraluminous side of the ternary diagram where $R \leqslant 1$, it is convenient to write the glass composition as

TABLE III. Parameters given by the GYZAS model for $(\text{MgO})_x(\text{Al}_2\text{O}_3)_y(\text{SiO}_2)_{1-x-y}$ glasses [15]. N_α refers to the number of atoms of type α, e.g., N_T refers to the total number of Si and Al atoms in tetrahedral units. Charge compensating (cc) and network modifying (m) Mg atoms are distinguished. The fraction of BO atoms is given by $f_\text{BO} = N_\text{BO}/N_\text{O} = 1 - f_\text{NBO}$.

Parameter	$R \leqslant 1$	$R \geqslant 1$
$f_\text{Al(IV)} = N_\text{Al(IV)}/N_\text{Al}$	$(y + px)/2y$	$(1 + p)/2$
$f_\text{NBO} = N_\text{NBO}/N_\text{O}$	$2(x + y - 2px)/(2 - x + y)$	$2(x + y - 2py)/(2 - x + y)$
N_NBO/N_Si	$2(x + y - 2px)/(1 - x - y)$	$2(x + y - 2py)/(1 - x - y)$
N_NBO/N_T	$2(x + y - 2px)/(1 - x + px)$	$2(x + y - 2py)/(1 - x + py)$
$N_\text{BO}/N_\text{T} = N_\text{O}(1 - f_\text{NBO})/N_\text{T}$	$[2 - x(3 - 4p) - y]/(1 - x + px)$	$[2 - 3x - y(1 - 4p)]/(1 - x + py)$
N_NBO/N_Mg	$2(x + y - 2px)/x$	$2(x + y - 2py)/x$
$N_\text{NBO}/(N_\text{Mg} + N_\text{Al}_\text{mcc})$	$2(x + y - 2px)/[x(1 - p) + y]$	$2(x + y - 2py)/[x + (1 - p)y]$
$f_\text{Mgcc} = N_\text{Mgcc}/N_\text{Mg}$	p	py/x
$f_\text{Mgm} = 1 - f_\text{Mgcc}$	$1 - p$	$(x - py)/x$
$f_\text{Al}_\text{mcc}:\text{Mg+Al} = N_\text{Al}_\text{mcc}/(N_\text{Mg} + N_\text{Al})$	$(y - px)/(x + 2y)$	$(1 - p)y/(x + 2y)$

$[(\text{MgO})(\text{Al}_2\text{O}_3)]_{px}[(\text{MgO})(\text{SiO}_2)]_{(1-p)x}[(\text{Al}_2\text{O}_3)(\text{SiO}_2)]_{y-px}$ $(\text{SiO}_2)_{1-2x-2y+2px}$ and to consider the reaction scheme [15]

$$px(\text{MgO} + \text{Al}_2\text{O}_3) + (1 - p)x(\text{MgO} + \text{SiO}_2)$$
$$+ (y - px)(\text{Al}_2\text{O}_3 + \text{SiO}_2) + (1 - 2x - 2y + 2px)(\text{SiO}_2)$$
$$\rightarrow px(\text{Mg}^{2+} + 2[\text{AlØ}_{4/2}]^-)$$
$$+ (1 - p)x(\text{Mg}^{2+} + [\text{SiØ}_{2/2}\text{O}_2]^{2-})$$
$$+ (y - px)([\text{AlØ}_{4/2}]^- + \text{Al}^{3+} + [\text{SiØ}_{2/2}\text{O}_2]^{2-})$$
$$+ (1 - 2x - 2y + 2px)\text{SiØ}_{4/2}. \tag{9}$$

In this case, there is no reaction between MgO and SiO_2 when $p = 1$ and all the Mg^{2+} ions play a charge-compensating role.

The parameters delivered by the GYZAS model are summarized in Table III. As discussed in Ref. [15], the model allows for reaction schemes other than those described by Eqs. (5)–(7). In this way, the NBO atoms can be associated with either the Si or Al(IV) atoms. Each BO atom has a half share in two T-centered tetrahedral units [T = Si or Al(IV)], so the number of T-BO linkages per T-centered tetrahedron is given by $\langle n \rangle = 2N_\text{BO}/N_\text{T}$. In this way, the total number of T-O linkages per T-centered tetrahedron is given by $N_\text{NBO}/N_\text{T} + 2N_\text{BO}/N_\text{T} = 4$, as required.

One of the key predictions of the GYZAS model is the dependence of the fraction of NBO atoms f_NBO on p and the glass composition. The value of p is linearly related to the cation field strength [15]. In the case of aluminosilicate glasses containing Na^+, K^+, Ca^{2+} or Ba^{2+}, f_NBO has been measured by ^{17}O triple-quantum MAS NMR experiments [51–53] or calculated in molecular dynamics simulations validated against ^{17}O multiple-quantum MAS NMR experiments [54]. A one-to-one correspondence is found between the measured or simulated values of f_NBO and those calculated from the GYZAS model [15].

In the scenario when all the NBO atoms are associated with Si atoms, the mean number of Si-BO bonds per Si-centered tetrahedron is given by $\langle n \rangle = 4 - N_\text{NBO}/N_\text{Si}$, which defines the average $Q^{\langle n \rangle}$ speciation of the silicon atoms. In this case, the number of Si-NBO bonds $N_\text{Si-NBO} = N_\text{NBO}$ and the total number of Si-O bonds $N_\text{Si-O} = 4N_\text{Si}$, so the probability of an Si-NBO bond is given by $p_\text{Si-NBO} = N_\text{NBO}/4N_\text{Si}$. The fraction of each Si Q^n species, where n denotes the number of BO

atoms per silicon atom, can then be estimated by assuming a binomial distribution of Si-BO and Si-NBO bonds such that

$$f_{Q^n} = \frac{4!}{n!(4-n)!}(1 - p_\text{Si-NBO})^n p_\text{Si-NBO}^{(4-n)}. \tag{10}$$

For the MgAS system, the mean value $\langle f_\text{Al(IV)} \rangle = 0.885(60)$ has been obtained from ^{27}Al MAS NMR experiments in the regime where $R \geqslant 1$, which gives $p = 2\langle f_\text{Al(IV)} \rangle - 1 = 0.77(11)$ [15]. These values are, within the experimental error, consistent with the results listed in Table I, which give $\langle f_\text{Al(IV)} \rangle = 0.893(33)$ and $p = 0.79(7)$. The composition dependence of the GYZAS model parameters is shown in Fig. 10 for the 50 and 60 mol% silica tie lines.

VI. DISCUSSION

The R dependence of the Si-O bond length is shown in Fig. 11(a). There is little variation with the glass composition, and the overall mean value $\langle \bar{r}_\text{SiO} \rangle = 1.622(7)$ Å is consistent with a tetrahedral coordination environment for the silicon atoms. There is a small but systematic variation of the Si-O bond length along the tectosilicate tie line for the largest silica content glasses, which will be discussed in Sec. VI F. In comparison, the Al-O bond length increases in value as $R \rightarrow 0$ in the peraluminous regime [Fig. 11(b)].

The R dependence of the Mg-O bond distance is shown in Fig. 11(c). Here, the first peak in the Mg-O correlations is broad and asymmetric (see, e.g., Figs. 7–9), which is consistent with the results obtained for selected glass compositions from experiments using NDIS [18]. The peak shape is indicative of a wide range of geometries for the coordination environment of magnesium, and is consistent with a broad distribution of electric-field gradient components at the magnesium position as inferred from solid-state ^{25}Mg NMR spectra [18,55]. In consequence, it was necessary to use two or three Gaussian functions to represent the first Mg-O peak. The weighted mean bond distance

$$\bar{r}_\text{MgO} = \frac{\int_{r_1}^{r_2} dr\, r g_\text{MgO}(r)}{\int_{r_1}^{r_2} dr\, g_\text{MgO}(r)} \tag{11}$$

is therefore plotted in Fig. 11(c), where $g_\text{MgO}(r)$ was obtained by summing the contributions from each of the fitted Gaussian functions, and r_1 and r_2 define the overall r-space extent of the
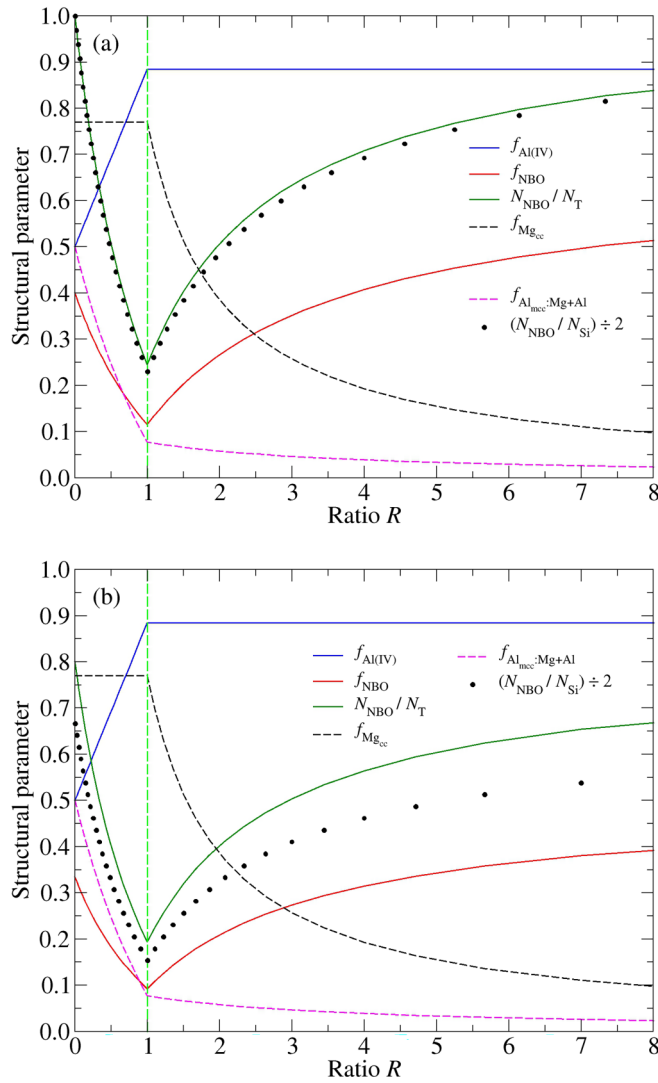
FIG. 10. Predictions of the GYZAS structural model for glassy MgAS along the (a) 50 mol% and (b) 60 mol% silica tie lines for $p = 0.77$. The same value of p is used across the entire R range. The green vertical broken line marks $R = 1$.

first peak. The results show a larger mean Mg-O bond distance in the peraluminous regime where the GYZAS model predicts a predominantly charge-compensating role for the Mg^{2+} ions.

In the peraluminous regime, the Al-O coordination numbers obtained from the ^{27}Al MAS NMR experiments increase in value as $R \to 0$ [Fig. 12(a)]. The exception is the small value $\bar{n}^O_{Al} = 4.06(5)$ for the silica-rich MgAS_7_76 glass at $R = 0.412$, which will be discussed in Sec. VI G. In comparison, the Mg-O coordination numbers obtained from the diffraction experiments indicate a roughly constant value with an average $\langle \bar{n}^O_{Mg} \rangle = 5.18(37)$ [Fig. 12(b)]. There is, however, a spread about the mean that will reflect, in part, the increasing difficulty in measuring the Mg-O coordination number by diffraction as the magnesia content of the glass decreases. There may also be some composition dependent change to the coordination environment. For example, a small value of $\bar{n}^O_{Mg}$ in the range 4.04–4.56 is found for glassy MgAS_10_50 ($R = 0.25$), which sits at the edge of glass-forming ability. This
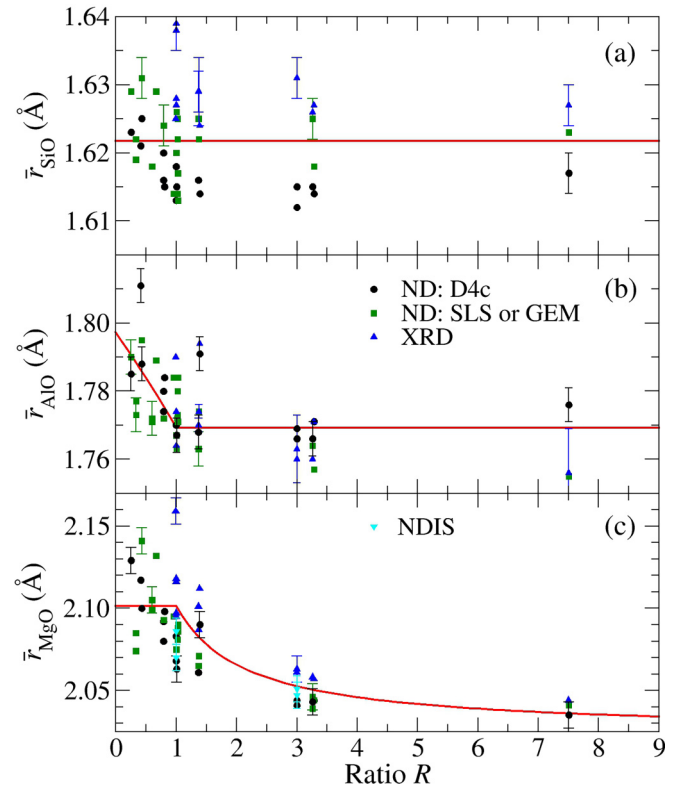

FIG. 11. Dependence of the (a) Si-O, (b) Al-O, and (c) Mg-O bond distances on the ratio R. The data sets were obtained from the diffraction experiments of the present work and, in (c), NDIS [18]. The Mg-O values were calculated using Eq. (11). The vertical lines show representative error bars. The red solid curves show (a) the average Si-O bond distance $\langle \bar{r}_{SiO} \rangle = 1.622(7)$ Å or (b) and (c) the predictions of the GYZAS model.
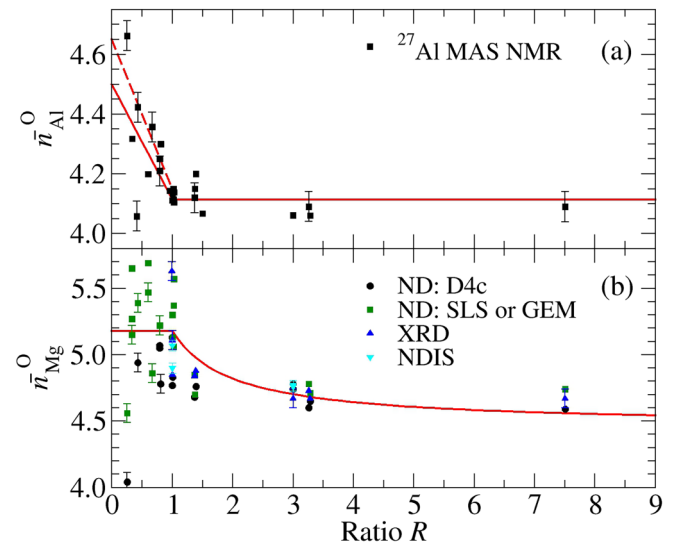

FIG. 12. Dependence of the (a) Al-O and (b) Mg-O coordination numbers on the ratio R. The data sets were obtained from (a) the ^{27}Al MAS NMR experiments (Table I) or (b) the diffraction experiments of the present work and NDIS [18]. The vertical lines show representative error bars. The red solid curves show the predictions of the GYZAS model. In (a), the red broken curve shows the effect of increasing $\bar{n}^O_{Al(V+)}$ from 5 to 5.3 in the regime where $R \leqslant 1$.

TABLE IV. The Al-O and Mg-O coordination numbers and bond distances obtained by fitting the measured data sets using the GYZAS model. The ratio of the longest to shortest Al-O or Mg-O bond distances is also given.

Atom pair α-β	$\bar{n}_\alpha^\beta$	$\bar{r}_{\alpha\beta}$ (Å)	Ratio
Al(IV)-O	4[a]	1.760(5)	–
Al(V)-O	5[a]	1.827(5)	1.04
Mg_m-O	4.46(9)	2.024(10)	–
Mg_{cc}-O	5.39(10)	2.120(10)	1.05

[a]Fixed parameter.

material corresponds to the most alumina-rich composition along the 50 mol% silica tie line and was made by containerless processing.

Overall, the R dependence of the Al-O and Mg-O bond distances and coordination numbers indicate a change in behavior when $R = 1$. Accordingly, the GYZAS model was used to interpret the results.

A. R dependence of the aluminum coordination environment

The fraction of aluminum atoms with an Al-O coordination number of five or greater is given by $f_{Al(V+)} = 1 - f_{Al(IV)}$. The mean Al-O coordination number follows from

$$\bar{n}_{Al}^O = f_{Al(IV)}\bar{n}_{Al(IV)}^O + f_{Al(V+)}\bar{n}_{Al(V+)}^O, \quad (12)$$

where $\bar{n}_{Al(IV)}^O = 4$ and $5 \leqslant \bar{n}_{Al(V+)}^O \leqslant 6$. The difference between the coordination numbers should lead to an Al(V+)-O bond distance $\bar{r}_{Al(V+)O}$ that is longer than the Al(IV)-O bond distance $\bar{r}_{Al(IV)O}$ because more oxygen atoms must cram into the first coordination shell of aluminum. Both distances will contribute to the position of the Gaussian peak fitted to the diffraction data. The weighted mean Al-O distance is given by

$$\bar{r}_{AlO} = \frac{f_{Al(IV)}\bar{n}_{Al(IV)}^O\bar{r}_{Al(IV)O} + f_{Al(V+)}\bar{n}_{Al(V+)}^O\bar{r}_{Al(V+)O}}{f_{Al(IV)}\bar{n}_{Al(IV)}^O + f_{Al(V+)}\bar{n}_{Al(V+)}^O}. \quad (13)$$

The individual Al-O bond distances were obtained from a least squares fit of Eq. (13) to the measured values shown in Fig. 11(b) for the regime where $R < 1$, subject to the conditions that (i) the same value $p = 0.77$ applies across the entire composition range, (ii) there are no Al(VI) species such that $\bar{n}_{Al(V+)}^O = \bar{n}_{Al(V)}^O = 5$, (iii) the bond distances are constrained such that Eq. (13) gives the mean value $\langle \bar{r}_{AlO} \rangle = 1.769(9)$ Å found from the diffraction experiments for the regime where $R \geqslant 1$, and (iv) $f_{Al(IV)}$ is given by the GYZAS model in both composition regimes (Table III). The fitted function is shown in Fig. 11(b) and the fitted distances are listed in Table IV. The distances are in accord with those typically found from experiment [56] or bond-valence theory [57], which give $\bar{r}_{Al(IV)O} = 1.74$–1.76 Å versus $\bar{r}_{Al(V)O} = 1.81$–1.84 Å.

The R dependence of $\bar{n}_{Al}^O$, calculated from Eq. (12) using the GYZAS model with $\bar{n}_{Al(V+)}^O = \bar{n}_{Al(V)}^O = 5$, is shown in Fig. 12(a). In the peraluminous regime, the majority of the measured $\bar{n}_{Al}^O$ values are larger than predicted by the model. The latter gives a maximal value at $R = 0$, where $f_{Al(IV)} = f_{Al(V+)} = 1/2$, such that $\bar{n}_{Al}^O = 4.5$. The maximum can be increased by invoking Al(VI) species, and the agreement

of the model with experiment can be improved by taking $\bar{n}_{Al(V+)}^O = 5.3$ for the regime where $R < 1$ [Fig. 12(a)]. This value of $\bar{n}_{Al(V+)}^O$ corresponds, however, to 15 mol% of the aluminum as Al(VI) species, which is substantially larger than indicated by the ^{27}Al MAS NMR results (Table I). Alternatively, more Al(V) atoms could be generated in the peraluminous regime by giving more weighting to the reaction scheme of Eq. (7) through an adjustment of the parameter p [15].

Threefold coordinated oxygen atoms in tricluster conformations may also contribute towards the glass structure. In their original conception, a tricluster oxygen atom is shared between three tetrahedral SiO_4 and/or AlO_4 motifs [58]. This oxygen atom can also be associated with higher coordinated aluminum atoms, provided the original concept is generalized such that an Al(IV) centered unit is replaced by an edge-sharing Al(V) or Al(VI) centered unit [59]. In ensuring charge neutrality, oxygen triclusters offer an alternative to NBO atoms for generating negatively charged units. As discussed in Sec. VI G, there is the possibility that their existence is signaled by the behavior of f_{NBO} in the peraluminous regime [15].

B. R dependence of the magnesium coordination environment

Figures 11(c) and 12(b) indicate that the Mg-O coordination number and bond distance both increase as R decreases from the limit $R \to \infty$, where the glass contains no alumina and all the Mg^{2+} ions take a network-modifying role, to the value $R = 1$, where most of the Mg^{2+} ions take a charge-compensating role (Fig. 10). In this progression, the ratio N_{NBO}/N_{Mg} decreases and is a minimum at the $R = 1$ tectosilicate composition (Table III). The results therefore suggest a difference between the average coordination environments of charge-compensating versus network-modifying Mg^{2+} ions that is related to the availability of NBO atoms. In general, both BO and NBO atoms will contribute towards these coordination environments. There is, however, a greater probability of NBO atoms contributing in the $R \to \infty$ limit, indicating that the higher charge on NBO versus BO atoms favors a more compact coordination environment for the network-modifying species. Conversely, there is a smaller probability of NBO atoms contributing when $R = 1$, leading to a less compact coordination environment for the charge-compensating species. Indeed, the probability of NBO atoms contributing towards the Mg^{2+} coordination environment would be vanishingly small at $R = 1$ if $p = 1$. Between these R limits, it is possible that a given Mg^{2+} ion will have in its first coordination sphere both Si NBO atoms and oxygen atoms from $[AlØ_{4/2}]^-$ units, and will therefore play a dual network-modifying/charge-compensating role.

In the following, it will be assumed that the composition dependence of the magnesium coordination environment can be described by a superposition of Mg^{2+} ions that take either a predominantly network-modifying or charge-compensating role. In this way, the mean coordination numbers and bond distances of these species can be estimated by applying the GYZAS model to the measured data sets.

The mean Mg-O coordination number is given by

$$\bar{n}_{Mg}^O = f_{Mg_{cc}}\bar{n}_{Mg_{cc}}^O + f_{Mg_m}\bar{n}_{Mg_m}^O, \quad (14)$$

where the subscripts cc and m denote the charge-compensating and network-modifying species, respectively, and the fractions $f_{Mg_{cc}}$ and f_{Mg_m} are predicted by the GYZAS model (Table III). The value of $\bar{n}_{Mg}^O$ should therefore be invariant within the $R \leqslant 1$ regime. The individual Mg-O coordination numbers were obtained from a least squares fit of Eq. (14) to the measured values shown in Fig. 12(b) for the regime where $R \geqslant 1$, subject to the conditions that (i) the same value $p = 0.77$ applies across the entire composition range, and (ii) the coordination numbers are constrained such that Eq. (14) gives the mean value $\langle \bar{n}_{Mg}^O \rangle = 5.18(37)$ found from experiment for the regime where $R < 1$ (in calculating this mean, extreme values were omitted, e.g., those obtained for the high-silica content tectosilicate glasses.) The fitted coordination numbers are listed in Table IV.

The weighted mean Mg-O distance is given by

$$\bar{r}_{MgO} = \frac{f_{Mg_{cc}} \bar{n}_{Mg_{cc}}^O \bar{r}_{Mg_{cc}O} + f_{Mg_m} \bar{n}_{Mg_m}^O \bar{r}_{Mg_mO}}{f_{Mg_{cc}} \bar{n}_{Mg_{cc}}^O + f_{Mg_m} \bar{n}_{Mg_m}^O}. \quad (15)$$

The individual Mg-O bond distances were obtained from a least squares fit of Eq. (15) to the measured values shown in Fig. 11(c) over the entire composition regime, with the coordination numbers $\bar{n}_{Mg_{cc}}^O$ and $\bar{n}_{Mg_m}^O$ set at the values found above. The fitted function is shown in Fig. 11(c) and the fitted values are listed in Table IV. The Mg$_{cc}$-O bond distance is longer than its Mg$_m$-O counterpart, which is consistent with the larger Mg$_{cc}$-O coordination number. For comparison, the Mg-O bond distance predicted by bond-valence theory [57] is 1.990(8) Å for $\bar{n}_{Mg}^O = 4.46(10)$ versus 2.067(7) Å for $\bar{n}_{Mg}^O = 5.39(10)$.

We note that the findings of this section contrast with the results of Guignard and Cormier [60], who argue for an invariant coordination number $\bar{n}_{Mg}^O \simeq 5.1(1)$ on the basis of the reverse Monte Carlo models obtained from neutron and x-ray diffraction data sets.

C. Experimental uncertainties

As mentioned above, there is a spread in the R dependence of the data points in Figs. 11 and 12 that is especially noticeable in the peraluminous regime. In particular, the spread is larger than the precision of the measurements, which is indicated by the size of the error bars. This behavior could originate from factors that include the (i) composition dependence of the glass forming ability, (ii) quench rate used to form the glass, (iii) silica content of the glass, (iv) procedure used to anneal the glass, (v) quality of the ^{27}Al MAS NMR data and sophistication of the modeling procedure used to interpret the measured spectra, and (vi) validity of the scheme used to interpret the measured total pair-distribution functions $D'_N(r)$ and $D'_X(r)$. In the peraluminous regime, for example, the glasses are often at the edge of glass-forming ability, requiring the use of containerless processing with fast quench-rates to avoid relaxation into the crystalline state.

To investigate the spread in values that originates from the silica content of the glass, the compositional trends along the tie lines with 50 and 60 mol% silica are investigated in Secs. VI D and VI E, respectively. Here, the methodology used to fit the diffraction data is validated by comparison with the results obtained by applying neutron diffraction with
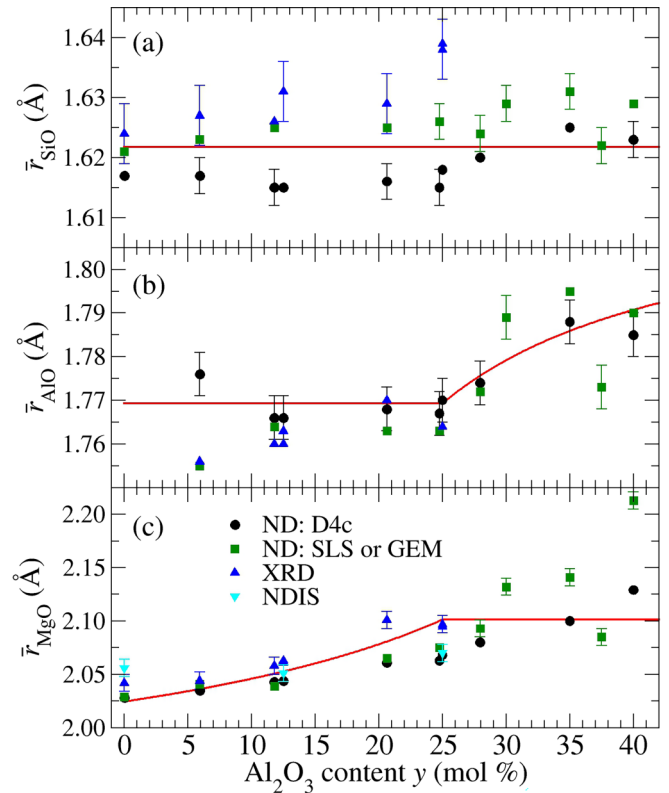

FIG. 13. Dependence of the (a) Si-O, (b) Al-O, and (c) Mg-O bond distances on the mol% of alumina along the tie line with 50 mol% silica. The data sets were obtained from the diffraction experiments of the present work and, in (c), NDIS [18]. The Mg-O values were calculated using Eq. (11). The vertical lines show representative error bars. The red solid curves show (a) the average Si-O bond distance for all compositions $\langle \bar{r}_{SiO} \rangle = 1.622(7)$ Å or (b) and (c) the predictions of the GYZAS model.

magnesium isotope substitution to selected glass compositions, a technique that removes much of the ambiguity associated with the interpretation of total pair-distribution functions [18]. The compositional trends along the tectosilicate tie line are considered in Sec. VI F. These tie lines were chosen for consideration because they correspond to the maximal amount of experimental information.

D. 50 mol% silica tie line

Figure 13 shows the composition dependence of the Si-O, Al-O, and Mg-O bond distances along the tie line with 50 mol% silica. The composition is represented by mol% alumina to enable the data points for zero alumina content (corresponding to the limit $R \to \infty$) to be plotted. The Si-O distance does not show a systematic change with the glass composition and the values are similar to the mean value obtained for all compositions $\langle \bar{r}_{SiO} \rangle = 1.622(7)$ Å. The Al-O and Mg-O distances predicted by the GYZAS model are in accord with experiment, showing a change in behavior at the 25 mol% alumina composition where $R = 1$. Figure 14 shows the composition dependence of the Al-O and Mg-O coordination numbers. Again, the model predicts the observed change in behavior at $R = 1$. The measured $\bar{n}_{Al}^O$ values in the
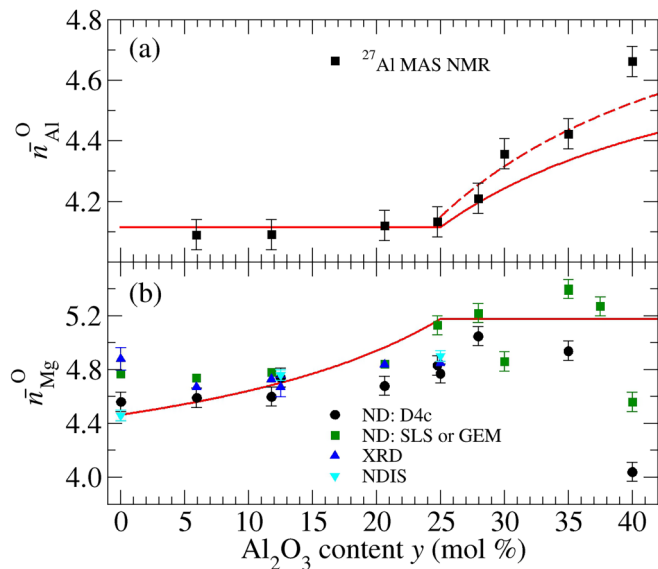
FIG. 14. Dependence of the (a) Al-O and (b) Mg-O coordination numbers on the mol% of alumina along the tie line with 50 mol% silica. The data sets were obtained from (a) the ^{27}Al MAS NMR experiments or (b) the diffraction experiments of the present work and NDIS [18]. The vertical lines show representative error bars. The red solid curves show the predictions of the GYZAS model. In (a), the red broken curve for the peraluminous regime shows the effect of increasing $\bar{n}^O_{Al(V+)}$ from 5 to 5.3.

peraluminous regime are better represented by the model if $\bar{n}^O_{Al(V+)}$ is increased from 5 to 5.3. The results show a small value $\bar{n}^O_{Mg} = 4.04$–4.56 for the MgAS_10_50 glass with the highest alumina content.

E. 60 mol% silica tie line

Figure 15 shows the composition dependence of the Si-O, Al-O, and Mg-O bond distances along the tie line with 60 mol% silica. The Si-O distances do not show a systematic change with the glass composition. The Al-O and Mg-O distances predicted by the GYZAS model are similar to experiment, showing a change in behavior at the 20 mol% alumina composition where $R = 1$. Figure 16 shows the composition dependence of the Al-O and Mg-O coordination numbers. Again, the model predicts the trends shown in the experimental data, including the change in behavior at $R = 1$. In the peraluminous regime, an increase in $\bar{n}^O_{Al(V+)}$ from 5 to 5.3 does not improve the agreement of the model with the measured values of $\bar{n}^O_{Al}$.

F. Tectosilicate tie line

Figure 17 shows the composition dependence of the Si-O, Al-O, and Mg-O bond distances along the tectosilicate tie line where $R = 1$. Here, the GYZAS model predicts an Al-O distance in agreement with experiment when the silica content $\leqslant 70$ mol%, but underestimates this distance for the compositions that are more silica-rich. In comparison, the measured $\bar{r}_{MgO}$ values do not change with composition, and the mean value $\langle \bar{r}_{MgO} \rangle = 2.09(2)$ Å is in agreement with the value 2.10 Å obtained from the GYZAS model.
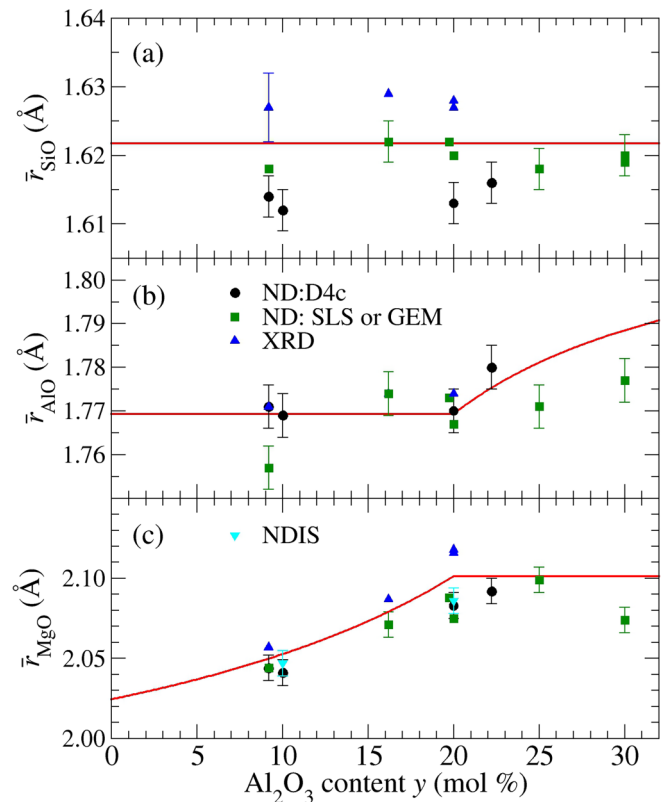

FIG. 15. Dependence of the (a) Si-O, (b) Al-O, and (c) Mg-O bond distances on the mol% of alumina along the tie line with 60 mol% silica. The data sets were obtained from the diffraction experiments of the present work and, in (c), NDIS [18]. The Mg-O values were calculated using Eq. (11). The vertical lines show representative error bars. The red solid curves show (a) the average Si-O bond distance for all compositions $\langle \bar{r}_{SiO} \rangle = 1.622(7)$ Å or (b) and (c) the predictions of the GYZAS model.

Figure 18 shows the composition dependence of the Al-O and Mg-O coordination numbers. The aluminum atoms are in a predominantly tetrahedral coordination environment across the entire composition range, which indicates that the majority of Mg^{2+} ions are involved in a charge-compensating role. There is uncertainty in the measured Mg-O coordination numbers when the silica content $\gtrsim 70$ mol%. The peak fitting procedure shows a marked increase in $\bar{n}^O_{Mg}$ with the silica content, which is unexpected because the measured mean Mg-O bond distance does not change with composition. The value $\bar{n}^O_{Mg} \simeq 8$ is obtained for the glass with the largest silica content, so a bond distance closer to $\bar{r}_{MgO} = 2.21$–2.27 Å is anticipated from experiment (Table II) or bond-valence theory [57]. This outcome likely originates from the decreased sensitivity of $D'(r)$ to the Mg-O correlations with increasing silica content (Fig. 9 and Fig. S11 [38]). Smaller $\bar{n}^O_{Mg}$ values are obtained by smoothing $rD'(r)$ with a Lorch modification function [61] and using Eq. (S2) [38] to consider the area under its first peak [Fig. 18(b)].

Overall, the results for the tectosilicate tie line indicate a change in the glass structure when the silica content exceeds $\simeq 70$ mol%. The Al-O bond length increases with the silica content as the Si-O bond length decreases towards the value
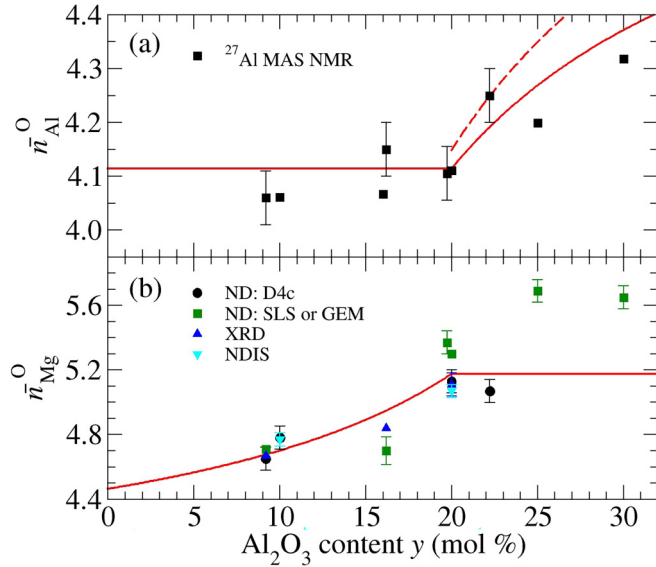
FIG. 16. Dependence of the (a) Al-O and (b) Mg-O coordination numbers on the mol% of alumina along the tie line with 60 mol% silica. The data sets were obtained from (a) the ^{27}Al MAS NMR experiments or (b) the diffraction experiments of the present work and NDIS [18]. The vertical lines show representative error bars. The red solid curves show the predictions of the GYZAS model. In (a), the broken red curve shows the effect of increasing $\bar{n}^O_{Al(V+)}$ from 5 to 5.3.

found for silica glass. These changes presumably reflect a decrease in the number of Si-O-Al linkages as the alumina content of the glass diminishes. They may also be related to a loss of Al(IV)-NBO linkages: ^{17}O NMR experiments on calcium aluminosilicate glasses [62] indicate a loss of these linkages when $N_{Si}/(N_{Al} + N_{Si}) > 0.49$ while ^{27}Al NMR experiments on strontium aluminosilicate glasses [63] indicate their loss when $N_{Si}/(N_{Al} + N_{Si}) \gtrsim 0.7$.

The structural changes along the tectosilicate tie line accompany the transformation of the mechanical properties of the glass from "normal" to "anomalous" [64], in that the mechanism of deformation on sharp contact loading changes from shear flow to densification as the silica content is increased beyond $\simeq 70$ mol% [16]. Such silica-rich glasses often exhibit unusually small values for the coefficient of thermal expansion [65]. As discussed in Sec. VII, the change in structure also coincides with a minimum in the glass hardness around 70 mol% silica as measured in nanoindentation experiments [16].

G. Network connectivity: fraction of NBO atoms

In the scenario where all the Si, Al(IV), and O atoms contribute towards the glass network, and the oxygen atoms within this network are either one-fold coordinated (NBO) or twofold coordinated (BO) to the Si/Al(IV) species, the fraction of NBO atoms can be found from the expression [15]

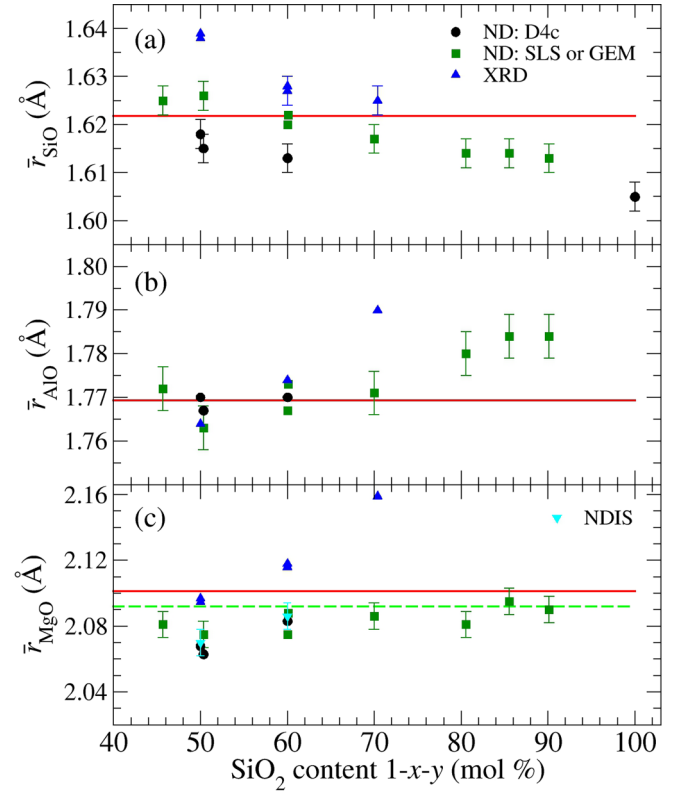$$f_{NBO} = 2 - \frac{c_{Si}}{c_O}\bar{n}^O_{Si} - f_{Al(IV)}\frac{c_{Al}}{c_O}\bar{n}^O_{Al(IV)}, \qquad (16)$$

FIG. 17. Dependence of the (a) Si-O, (b) Al-O, and (c) Mg-O bond distances on the mol% of silica along the tectosilicate tie line where $R = 1$. The data sets were obtained from the diffraction experiments of the present work and, in (c), NDIS [18]. The Mg-O values were calculated using Eq. (11). The vertical lines show representative error bars. The red solid curves show (a) the average Si-O bond distance for all compositions $\langle\bar{r}_{SiO}\rangle = 1.622(7)$ Å or (b) and (c) the predictions of the GYZAS model. In (c), the green broken curve gives the mean value $\langle\bar{r}_{MgO}\rangle = 2.09(2)$ Å obtained from the plotted data points.

where $\bar{n}^O_{Si} = \bar{n}^O_{Al(IV)} = 4$. The derivation of this equation makes no reference to the location of the NBO atoms, i.e., they can be associated with the Si and/or Al(IV) atoms.

Figures 19(a) and 19(b) show the R dependence of f_{NBO} calculated for the 50 and 60 mol% silica tie lines, respectively, using the $f_{Al(IV)}$ values taken from the ^{27}Al MAS NMR experiments (Table I). The predictions of the GYZAS model are in overall accord, although there is an indication for the 60 mol% tie line that the model overestimates the fraction of NBO atoms within the peraluminous regime.

Figure 19(c) shows the R dependence of the ratio $N_{NBO}/(N_{Mg} + N_{Al_{mcc}})$ for all the data sets listed in Table I. This ratio compares the availability of NBO atoms, which break the connectivity of the tetrahedral network, to the availability of high cation field-strength magnesium and Al_{mcc} ions, which may hold together the pieces of the network thus fragmented. The cation field strength is defined by $F_M = Z_M/r^2_M$, where Z_M is the formal charge on species M. Its value for aluminum and magnesium ions with different M-O coordination numbers is given in Table V. The ratio $N_{NBO}/(N_{Mg} + N_{Al_{mcc}}) \neq 0$ for the $R = 1$ tectosilicate compositions, in contradiction to the standard model for aluminosilicate glass (Sec. I).
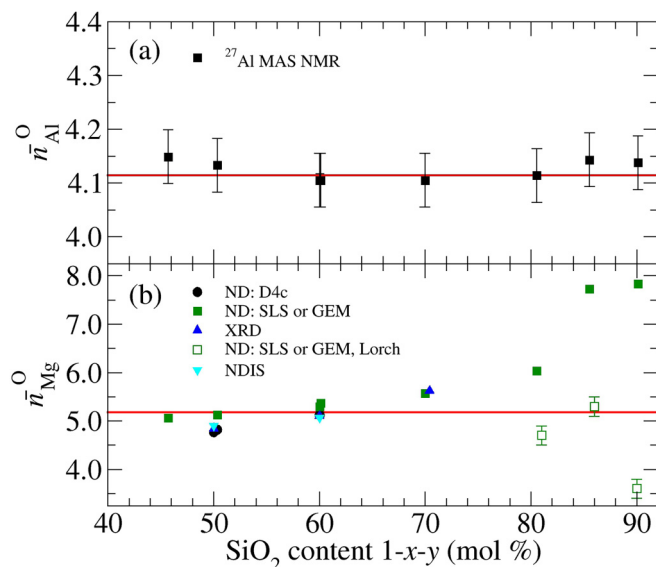
FIG. 18. Dependence of the (a) Al-O and (b) Mg-O coordination numbers on the mol% of silica along the tectosilicate tie line where $R = 1$. The data sets were obtained from (a) the ^{27}Al MAS NMR experiments or (b) the diffraction experiments of the present work by fitting $D'(r)$ (solid symbols) or by considering the area under the first peak in $rD'(r)$ after the application of a Lorch modification function (open symbols). In (b), the Mg-O distances from NDIS experiments are also shown [18]. In (a) the vertical lines show representative error bars and in (b) most of the error bars are comparable to the symbol size. The red solid curves show the predictions of the GYZAS model.

The GYZAS model represents the overall trends that are observed. An exception is the negative value of the ratio $N_{NBO}/(N_{Mg} + N_{Al_{mcc}})$ at $R = 0.412$, corresponding to the high silica content MgAS_7_76 glass for which $\bar{n}_{Al}^O = 4.06(5)$, i.e., to a peraluminous composition where the coordination environments of both Al and Si are predominantly tetrahedral. The corresponding Al-O bond distance $\bar{r}_{AlO} = 1.811(7)$ Å is large and close to the value of 1.835 Å predicted by bond-valence theory for Al(V) atoms [57]. The fraction of NBO atoms calculated from Eq. (16) also takes a negative value $f_{NBO} = -0.058(8)$, which points to a breakdown of the assumptions on which this equation is predicated. The unphysical value of f_{NBO} may indicate the presence of threefold coordinated oxygen atoms in tricluster conformations [15].

TABLE V. Cation field strength F_M for Al^{3+} and Mg^{2+} ions with different coordination numbers (CN). The ionic radii are taken from Shannon [66].

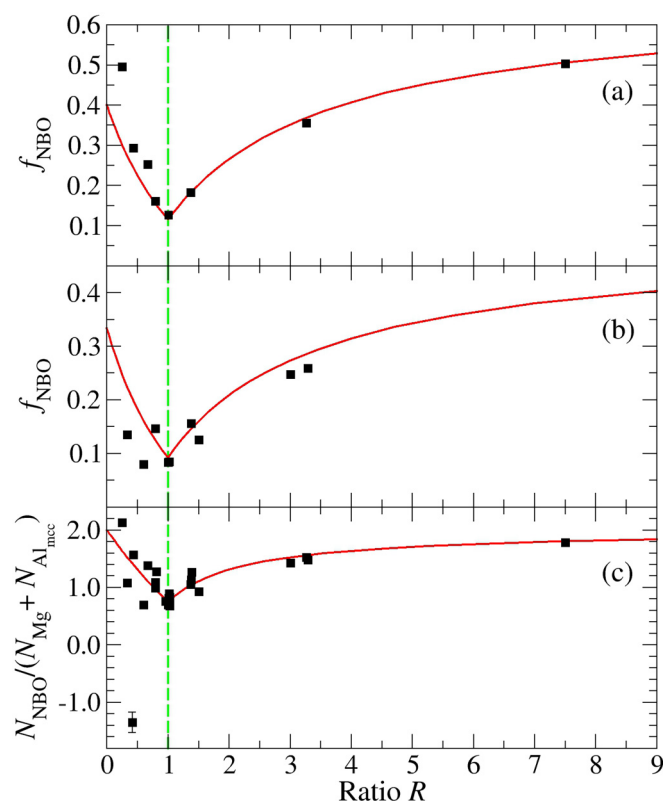| Ion	CN	r_M (Å)	F_M (Å^{-2})
Al^{3+}	4	0.39	13.15
	5	0.48	8.68
	6	0.535	6.99
Mg^{2+}	4	0.57	6.16
	5	0.66	4.59
	6	0.72	3.86
	8	0.89	2.52

FIG. 19. The R dependence of (a) f_{NBO} along the 50 mol% silica tie line, (b) f_{NBO} along the 60 mol% silica tie line, and (c) the ratio $N_{NBO}/(N_{Mg} + N_{Al_{mcc}})$. The green broken vertical line marks the $R = 1$ composition. The data sets (solid squares) were obtained from Eq. (16) with $f_{Al(IV)}$ taken from the ^{27}Al MAS NMR results listed in Table I. The red curves show the predictions of the GYZAS model with $p = 0.77$.

H. Does Mg^{2+} act as a network former?

In the above, the network is assumed to comprise all the Al(IV) and fourfold coordinated Si species and all the oxygen atoms. In this way, the fraction of NBO atoms can be predicted. For those aluminosilicate systems containing monovalent or divalent network-modifying/charge-compensating species for which this fraction is available from solid-state ^{17}O NMR experiments or molecular dynamics simulations validated against ^{17}O NMR experiments, agreement is found between the predicted and measured/modeled values (Sec. V).

It has been suggested that fourfold coordinated magnesium ions Mg(IV) can act as network formers. For instance, ^{29}Si MAS NMR experiments have been performed on bioglasses with the composition 49.46SiO$_2$-1.07P$_2$O$_5$-[23.08(1 − x)]CaO-xMgO-26.38Na$_2$O (x = 0–23.08 mol%) to measure the Q^n speciation [72]. The conversion of Q^2 to Q^3 Si species was observed on substituting Ca^{2+} for Mg^{2+}, leading to a loss of NBO atoms. This alteration to the network connectivity can be explained by invoking Mg(IV) atoms that act as network formers. Equation (16) can then be rewritten as

$$f_{NBO} = 2 - \frac{c_{Si}}{c_O}\bar{n}_{Si}^O - \frac{c_P}{c_O}\bar{n}_P^O - f_{Mg(IV)}\frac{c_{Mg}}{c_O}\bar{n}_{Mg(IV)}^O \quad (17)$$

TABLE VI. Percentage of Q^n species obtained from ^{29}Si MAS NMR experiments on glassy MgSiO$_3$, CaSiO$_3$ and CaMgSi$_2$O$_6$. The mean number of Si-BO bonds per Si atom $\langle n \rangle$ is also given, along with the ratio N_{NBO}/N_{Si}. The results are compared to a statistical distribution of Q^n species for a glass of composition MSiO$_3$, where M denotes Mg, Ca, or a mixture of both, as calculated using Eq. (10) with $p_{Si\text{-}NBO} = 0.5$.

Glass	Q^0	Q^1	Q^2	Q^3	Q^4	$\langle n \rangle$	N_{NBO}/N_{Si}	Reference
MgSiO$_3$	0.0	25.0	42.0	25.7	7.3	2.15	1.85	[67]
	1.4(1)	19.1(3)	53.0(4)	25.2(3)	1.4(1)	2.06	1.94	[68]
	0	26.0(5)	42.0(8)	24.0(5)	8.0(2)	2.14	1.86	[55]
CaSiO$_3$	0.72(13)	19.33(28)	54.68(34)	24.14(53)	1.13(1)	2.06	1.94	[69]
	0	20(5)	64(8)	14(5)	2(1)	1.98	2.02	[70]
	0	16.6	64.4	19.0	0.0	2.02	1.98	[71]
CaMgSi$_2$O$_6$	0	28(8)	43(10)	25(6)	4(1)	2.05	1.95	[70]
	0	33.0(8)	43.0(9)	20.0(4)	4.0(1)	1.95	2.05	[55]
MSiO$_3$	6.25	25	37.5	25	6.25	2	2	–

where $\bar{n}_{Si}^{O} = \bar{n}_{P}^{O} = \bar{n}_{Mg(IV)}^{O} = 4$ and $f_{Mg(IV)}$ is the fraction of magnesium atoms that take a network forming role. If it is assumed that $f_{Mg(IV)} = 1$, too few NBO atoms are generated. Instead, the value $f_{Mg(IV)} = 0.14$ leads to better accord with the measured N_{NBO}/N_{Si} values. The mean Mg-O coordination number was not, however, measured to try and assess the magnesium speciation. For example, a value of $\bar{n}_{Mg}^{O} = 4$ from diffraction would indicate that Mg(IV) atoms can play both a network-modifying and network-forming role, with only a small fraction adopting the latter.

In the MgAS glasses, if the Mg(IV) atoms act as network formers then Eq. (16) can be rewritten as

$$f_{NBO} = 2 - \frac{c_{Si}}{c_O}\bar{n}_{Si}^{O} - f_{Al(IV)}\frac{c_{Al}}{c_O}\bar{n}_{Al(IV)}^{O} - f_{Mg(IV)}\frac{c_{Mg}}{c_O}\bar{n}_{Mg(IV)}^{O}. \tag{18}$$

In these materials, the diffraction results show that $\bar{n}_{Mg}^{O} \gtrsim 4.6$ for the majority of glass compositions (Tables S6–S8 [38]). For $\bar{n}_{Mg}^{O} = 4.6$, the smallest value $f_{Mg(IV)} = 0.4$ is obtained by assuming that only Mg(IV) and Mg(V) species contribute towards the glass structure such that $\bar{n}_{Mg}^{O} = 4f_{Mg(IV)} + 5(1 - f_{Mg(IV)})$. This $f_{Mg(IV)}$ value is consistent with molecular dynamics simulations of glassy MgSiO$_3$ that give a good account of the Q^n speciation found from ^{29}Si MAS NMR experiments [6]. For $\bar{n}_{Mg}^{O} > 4.6$, the same assumptions lead to smaller values of $f_{Mg(IV)}$. The f_{NBO} values calculated for the various glass compositions of Table I using $f_{Mg(IV)} = 0.4$ are mostly negative. This finding is unphysical and implies that either (i) $f_{Mg(IV)}$ is too large or (ii) the assumptions leading to Eq. (18) are invalid.

Table VI shows the Q^n speciation observed in ^{29}Si MAS NMR experiments on glassy enstatite MgSiO$_3$, wollastonite CaSiO$_3$ and diopside CaMgSi$_2$O$_6$. The results are compared to a statistical distribution of Q^n species (Sec. V) and do not indicate different structural roles for the Mg^{2+} and Ca^{2+} ions. The measured ratio $N_{NBO}/N_{Si} \simeq 2$ is in accordance with both the GYZAS model and Eq. (16) where it is assumed that Mg^{2+} and Ca^{2+} do not act as network formers. In comparison, the measured $\bar{n}_{Mg}^{O}$ values for MgSiO$_3$ are in the range 4.56–4.88, which gives $f_{Mg(IV)}$ values in the range 0.12–0.44 if Mg(IV) and Mg(V) are the only magnesium species that contribute towards the glass structure. If these Mg(IV) atoms were deemed to be network-formers, Eq. (18) leads to N_{NBO}/N_{Si} values in

the range 0.24–1.52, which is not in agreement with experiment.

The absence of a network forming role for Mg^{2+} is supported by experiments in which the entropy of mixing S^{mix} was deduced from the viscosity measured along the pyroxene CaSiO$_3$-MgSiO$_3$ ($y = 0$), garnet Ca$_3$Al$_2$Si$_3$O$_{12}$-Mg$_3$Al$_2$Si$_3$O$_{12}$ ($y = 0.143$) and anorthite CaAl$_2$Si$_2$O$_8$-MgAl$_2$Si$_2$O$_8$ ($y = 0.25$) tie lines, where CaO was systematically replaced by MgO [73,74]. The experimental results are consistent with an ideal mixing hypothesis for the Ca^{2+} and Mg^{2+} cations, where the contribution of S^{mix} to the configurational entropy S^{config} is largest at temperatures near the glass transition temperature T_g.

We note that when magnesia is replaced by alumina, Al^{3+} ions with a large cation field-strength are introduced to the glass structure. The F_M values listed in Table V suggest that Al(V) would be a more effective network-forming candidate than Mg(IV).

To establish f_{NBO} and further test the validity of the GYZAS model and Eq. (16), it would be helpful to perform ^{17}O MAS NMR experiments on MgAS glasses. Such experiments would also indicate whether "free" oxide ions O^{2-} exist, as suggested from experiments on low silica content (Ca$_{0.5}$Mg$_{0.5}$O)$_{1-x}$(SiO$_2$)$_x$ ($0.28 \leqslant x \leqslant 0.33$) glasses [75]. These oxide ions are not bound to network-forming units but appear in M-O-M connections, where M denotes Ca or Mg.

I. Material properties

The network connectivity is expected to affect the structure-related material properties. Figure 20 shows, however, little change at $R = 1$ in the measured high-temperature shear viscosity along the tie lines with approximately 52, 67, or 75 mol% silica [76], where a minimum is expected in f_{NBO} and related structural parameters (Fig. 10). This observation may indicate that the structure of the glass is not representative of the structure of the high-temperature melt. Indeed, the sensitivity of the viscosity of aluminosilicates to composition and structure is much greater near the glass transition than above the liquidus where the data sets tend to converge [79].

Figure 21 shows the composition dependent changes that occur to the glass hardness H [77,78] and several of the structural parameters along the $\simeq 70$ mol% silica tie line. In
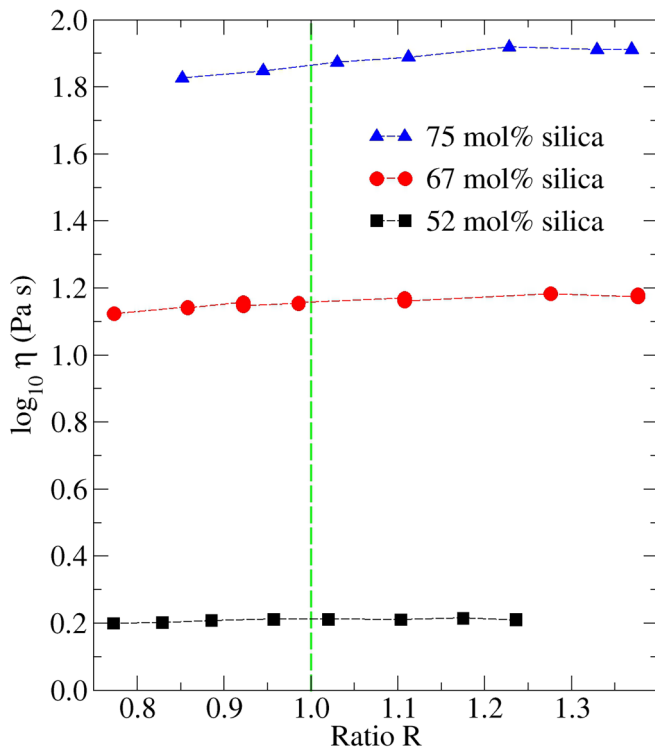
FIG. 20. Dependence of $\log_{10} \eta$ vs the ratio R for the tie lines with approximately 52, 67, and 75 mol% silica at a temperature of 1600 °C [76]. The green broken vertical line marks the $R = 1$ composition. For a given tie line, no change in behavior is observed at $R = 1$ where a minimum is expected in f_{NBO} and related structural parameters (Fig. 10).

FIG. 21. Dependence of (a) the microhardness [77,78], (b) N_{NBO}/N_T, (c) $N_{NBO}/(N_{Mg} + N_{Al_{mcc}})$, and (d) the mean Al-O coordination number $\bar{n}_{Al}^O$ on the ratio R along the $\simeq 70$ mol% silica tie line. The green broken vertical line marks the $R = 1$ composition. In (a), the blue broken curve is drawn as a guide for the eye. In (b)–(c), the solid circles with vertical error bars were calculated using Eq. (16) with $f_{Al(IV)}$ taken from the ^{27}Al MAS NMR results listed in Table I. The red curves show the predictions of the GYZAS model with $p = 0.77$. In (d), the data points are taken from Table I.

this comparison, it should be noted that the hardness and structural measurements were not made on an identical set of samples. Nevertheless, a minimum in H occurs around $R = 1$, which is associated with a minimum in N_{NBO}/N_T, i.e., to a maximum in the connectivity of the tetrahedral network. The minimum in H is also associated with a minimum in the ratio $N_{NBO}/(N_{Mg} + N_{Al_{mcc}})$ and a minimum in the Al-O coordination number $\bar{n}_{Al}^O$.

In these considerations, it is pertinent to point out that for the magnesium aluminosilicate system, the energetic distinction between the bonds involving Mg^{2+} and NBO or BO atoms is likely to be smaller than in commonly studied aluminosilicates, where network-modifying/charge-compensating cations such as Na^+ and Ca^{2+} have a lower field strength and weaker, more ionic interactions with the NBO atoms. The break in the predicted curves of speciation versus composition at $R = 1$ is thus likely to be less discontinuous than indicated by Fig. 10. Indeed, as compared to the sodium and calcium aluminosilicate systems, which are characterized by larger values for the parameter p, the transition in behavior at $R = 1$ is less sharply defined. For instance, f_{NBO} takes its minimal value of zero at $R = 1$ in the limit when $p = 1$, which corresponds to low field-strength cations [15], but takes a finite value at $R = 1$ for magnesium aluminosilicates where $p \simeq 0.77$ (Fig. 10). Similarly, a smearing of the discontinuity in $f_{Al(IV)}$ predicted by the GYZAS model at $R = 1$ might be anticipated, although the available ^{27}Al MAS NMR data on
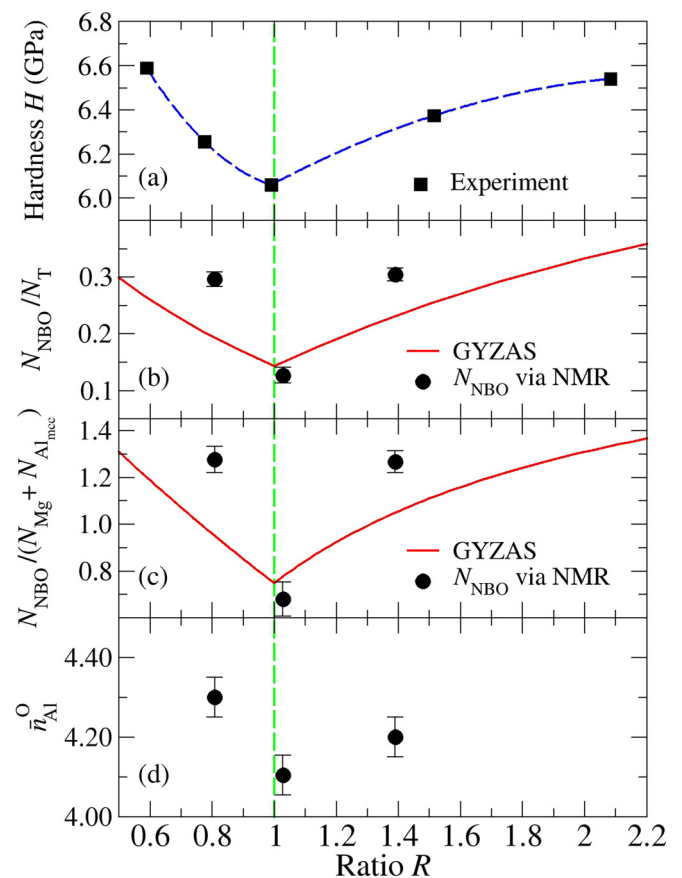
the magnesium aluminosilicate system do support the occurrence of an abrupt change at the $R = 1$ composition [15]. In view of the small number of data points, it is not possible to assess the sharpness of the transition in the hardness at $R = 1$ for the $\simeq 70$ mol% silica tie line (Fig. 21).

Figure 22 shows the composition dependent changes that occur to H [16] and several of the structural parameters along the tectosilicate tie line. Here, there is a minimum in H around 70 mol% silica that is not accompanied by an extremum in the connectivity of the tetrahedral network as expressed by N_{NBO}/N_T. There is a minimum, however, in the ratio $N_{NBO}/(N_{Mg} + N_{Al_{mcc}})$ and in the coordination number $\bar{n}_{Al}^O$. These minima are also related to the transition in the mechanism of deformation from shear flow to densification with increasing silica content (Sec. VIF).

VII. CONCLUSIONS

A comprehensive investigation was performed on the structure of MgAS glasses using neutron and x-ray diffraction,
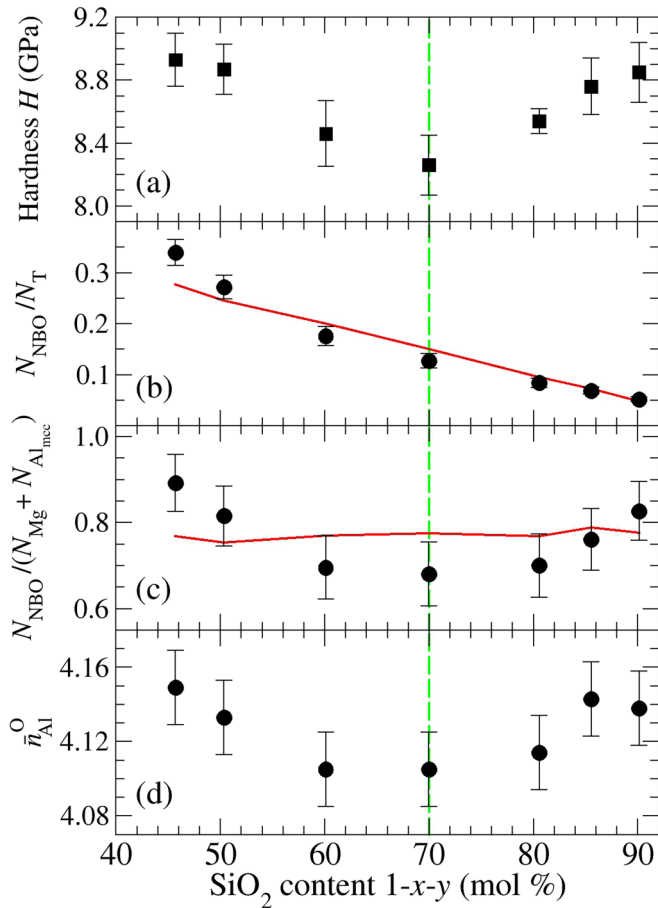
FIG. 22. Dependence of (a) the hardness measured in nanoindentation experiments using a Berkovich diamond tip [16], (b) N_{NBO}/N_T, (c) $N_{NBO}/(N_{Mg} + N_{Al_{mcc}})$, and (d) the mean Al-O coordination number $\bar{n}_{Al}^O$ on the mol% of silica for glasses on or near to the tectosilicate tie line. The green broken vertical line marks the minimum in H at about 70 mol% silica. In (b)–(c), the solid circles with vertical error bars were calculated using Eq. (16) with $f_{Al(IV)}$ taken from the ^{27}Al MAS NMR results listed in Table I. All measurements correspond to the same set of samples. The red curves show the predictions of the GYZAS model with $p = 0.77$. In (d), the data points are taken from Table I.

aided by the results obtained from ^{27}Al MAS NMR spectroscopy. The results were interpreted using the GYZAS model for aluminosilicate glasses [15]. The model contains a single adjustable parameter that was set to the value $p = 0.77$ found from the mean fraction of Al(IV) atoms observed in the $R \geqslant 1$ regime from ^{27}Al MAS NMR experiments [15].

The predicted R dependence for the fractions of fourfold and higher coordinated aluminum atoms was combined with the diffraction results to deliver Al(IV)-O and Al(V)-O bond distances in agreement with those expected from other experiments and bond-valence theory (Table IV). The predicted R dependence for the fractions of network-modifying and charge-compensating Mg^{2+} ions was also combined with the diffraction results, showing that these species are structurally inequivalent: The mean Mg-O coordination number and bond distance are larger for the charge-compensating species (Ta-

ble IV). A network forming role for Mg(IV) is improbable: It does not perform this role in MgSiO$_3$ or CaMgSi$_2$O$_6$ glass, and it is unlikely to adopt this role when alumina is added because the entropy of mixing S^{mix} of Ca^{2+} and Mg^{2+} along the garnet and anorthite tie lines is ideal.

At the boundaries of the glass-forming region, more exotic behavior can be observed. Along the tectosilicate tie line, for example, the Al-O bond distance increases as the Si-O bond distance decreases when the silica content exceeds $\gtrsim 70$ mol%, even though the Al-O and Si-O coordination numbers do not show any significant change. These structural changes accompany the transformation from a "normal" to "anomalous" glass, where the mechanism of deformation changes from shear flow to densification on sharp contact loading, and are associated with a minimum in the glass hardness at about 70 mol% silica [Fig. 22(a)]. Along the 50 mol% silica tie line, there appears to be a sudden drop in the Mg-O coordination number to $\bar{n}_{Mg}^O = 4.04$–4.56 for the glass with the largest alumina content.

The fraction of NBO atoms f_{NBO} was calculated from Eq. (16) using the $f_{Al(IV)}$ values measured using ^{27}Al MAS NMR spectroscopy. This approach assumes a glass network containing all the Si, Al(IV), and O atoms, where each oxygen atom plays either an NBO or BO role. For the peraluminous regime, the fraction of NBO atoms decreases as the silica content of the glass increases [Figs. 19(a) and 19(b)]. The calculated value of f_{NBO} takes an unphysical value for the 76 mol% silica glass MgAS_7_76, which indicates a breakdown of the assumptions on which Eq. (16) is predicated. Threefold coordinated oxygen atoms in tricluster conformations may therefore contribute towards the glass structure [15].

The high-temperature viscosity does not show a change in behavior when $R = 1$ along a tie line with either 52, 67, or 75 mol% silica (Fig. 20). The glass hardness is not related in a simple way to the network connectivity as expressed by N_{NBO}/N_T. Along the 70 mol% silica tie line, for example, the smallest hardness corresponds to a minimum in the composition dependence of N_{NBO}/N_T, i.e., to maximal connectivity of the tetrahedral motifs. No such relation exists along the tectosilicate tie line. In all cases, the minimum hardness does, however, coincide with a minimum in the composition dependence of both $\bar{n}_{Al}^O$ and the ratio $N_{NBO}/(N_{Mg} + N_{Al_{mcc}})$. The hardness appears to reflect a competition between the network-breaking effect of the NBO atoms versus the ability of the high cation field-strength magnesium and Al$_{mcc}$ ions to hold together the pieces of a fragmented network.

ACKNOWLEDGMENTS

[1] M. Dejneka and T. J. Kiczenski, in *Springer Handbook of Glass*, edited by J. D. Musgraves, J. Hu, and L. Calvez (Springer, Cham, Switzerland, 2019), Chap. 45, pp. 1519–1551.

[2] S. Jahn and P. A. Madden, Phys. Earth Planet. Inter. **162**, 129 (2007).

[3] *Magmas under Pressure*, edited by Y. Kono and C. Sanloup (Elsevier, Amsterdam, 2018).

[4] T. M. Gross, in *Springer Handbook of Glass*, edited by J. D. Musgraves, J. Hu, and L. Calvez (Springer, Cham, Switzerland, 2019), Chap. 8, pp. 273–296.

[5] X. Ke, Z. Shan, Z. Li, Y. Tao, Y. Yue, and H. Tao, J. Am. Ceram. Soc. **103**, 3600 (2020).

[6] P. S. Salmon, G. S. Moody, Y. Ishii, K. J. Pizzey, A. Polidori, M. Salanne, A. Zeidler, M. Buscemi, H. E. Fischer, C. L. Bull, S. Klotz, R. Weber, C. J. Benmore, and S. G. MacLeod, J. Non-Cryst. Solids: X **3**, 100024 (2019).

[7] S. K. Lee, J. L. Mosenfelder, S. Y. Park, A. C. Lee, and P. D. Asimow, Proc. Natl. Acad. Sci. U.S.A. **117**, 21938 (2020).

[8] M. P. Borom, C. A. Johnson, and L. A. Peluso, Surf. Coat. Technol. **86-87**, 116 (1996).

[9] C. Mercer, S. Faulhaber, A. Evans, and R. Darolia, Acta Mater. **53**, 1029 (2005).

[10] S. Krämer, S. Faulhaber, M. Chambers, D. R. Clarke, C. G. Levi, J. W. Hutchinson, and A. G. Evans, Mater. Sci. Eng. A **490**, 26 (2008).

[11] D. M. Beall and W. A. Cutler, Am. Ceram. Soc. Bull. **99**, 24 (2020).

[12] A. A. Reddy, A. Goel, D. U. Tulyaganov, S. Kapoor, K. Pradeesh, M. J. Pascual, and J. M. F. Ferreira, J. Power Sources **231**, 203 (2013).

[13] H. Sreenivasan, W. Cao, Y. Hu, Q. Xiao, M. Shakouri, M. Huttula, J. L. Provis, M. Illikainen, and P. Kinnunen, PLoS One **15**, e0244621 (2020).

[14] J. C. C. Freitas and M. E. Smith, Annu. Rep. NMR Spectrosc. **75**, 25 (2012).

[15] L. V. D. Gammond, R. E. Youngman, A. Zeidler, B. G. Aitken, and P. S. Salmon, J. Chem. Phys. **156**, 064503 (2022).

[16] L. A. Lamberson, Influence of atomic structure on plastic deformation in tectosilicate calcium-aluminosilicate, magnesium-aluminosilicate, and calcium-galliosilicate glasses, Ph.D. thesis, Cornell University, U.S.A., 2016.

[17] D. R. Neuville, L. Cormier, V. Montouillout, P. Florian, F. Millot, J.-C. Rifflet, and D. Massiot, Am. Mineral. **93**, 1721 (2008).

[18] H. Mohammadi, R. Mendes Da Silva, A. Zeidler, L. V. D. Gammond, F. Gehlhaar, M. de Oliveira, Jr., H. Damasceno, H. Eckert, R. E. Youngman, B. G. Aitken, H. F. Fischer, H. Kohlmann, L. Cormier, C. J. Benmore, and P. S. Salmon, J. Chem. Phys. **157**, 214503 (2022).

[19] L. Cormier and G. J. Cuello, Phys. Rev. B **83**, 224204 (2011).

[20] P. S. Salmon, A. C. Barnes, R. A. Martin, and G. J. Cuello, Phys. Rev. Lett. **96**, 235502 (2006).

[21] H. E. Fischer, A. C. Barnes, and P. S. Salmon, Rep. Prog. Phys. **69**, 233 (2006).

[22] D. Waasmaier and A. Kirfel, Acta Cryst. A **51**, 416 (1995).

[23] V. F. Sears, Neutron News **3**, 26 (1992).

[24] L. V. D. Gammond, H. Auer, R. Mendes Da Silva, A. Zeidler, J. F. Ortiz-Mosquera, A. M. Nieto-Muñoz, A. C. M. Rodrigues, I. d'Anciães Almeida Silva, H. Eckert, C. J. Benmore, and P. S. Salmon, J. Chem. Phys. **155**, 074501 (2021).

[25] D. I. Grimley, A. C. Wright, and R. N. Sinclair, J. Non-Cryst. Solids **119**, 49 (1990).

[26] E. Lippmaa, A. Samoson, and M. Mägi, J. Am. Chem. Soc. **108**, 1730 (1986).

[27] M. Yon, F. Fayon, D. Massiot, and V. Sarou-Kanian, Solid State Nucl. Magn. Reson. **110**, 101699 (2020).

[28] D. Massiot, F. Fayon, M. Capron, I. King, S. Le Calvé, B. Alonso, J.-O. Durand, B. Bujoli, Z. Gan, and G. Hoatson, Magn. Reson. Chem. **40**, 70 (2002).

[29] G. Le Caër and R. A. Brand, J. Phys.: Condens. Matter **10**, 10715 (1998).

[30] A. K. Soper, in *International Collaboration on Advanced Neutron Sources ICANS-XI*, edited by M. Misawa, M. Furusaka, H. Ikeda, and N. Watanabe (KEK, Tsukuba, Japan, 1991), pp. 809–819.

[31] A. C. Hannon, Nucl. Instrum. Methods Phys. Res., Sect. A **551**, 88 (2005).

[32] H. E. Fischer, G. J. Cuello, P. Palleau, D. Feltin, A. C. Barnes, Y. S. Badyal, and J. M. Simonson, Appl. Phys. A **74**, s160 (2002).

[33] A. K. Soper, *GudrunN and GudrunX*, Tech. Rep. (ISIS Facility, Rutherford Appleton Laboratory, Chilton, Didcot, Oxon, United Kingdom OX11 0QX, 2012).

[34] M. A. Howe, R. L. McGreevy, and W. S. Howells, J. Phys.: Condens. Matter **1**, 3433 (1989).

[35] P. S. Salmon, S. Xin, and H. E. Fischer, Phys. Rev. B **58**, 6115 (1998).

[36] A. P. Hammersley, J. Appl. Crystallogr. **49**, 646 (2016).

[37] X. Qiu, J. W. Thompson, and S. J. L. Billinge, J. Appl. Crystallogr. **37**, 678 (2004).

[38] See Supplemental Material at http://link.aps.org/supplemental/10.1103/PhysRevMaterials.6.125603 for (1) the parameters from the fitted line shapes for (a) both the central transition and spinning sidebands or (b) just the central transition of the ^{27}Al MAS NMR spectra, (2) several of the measured $S(k)$ and fitted $D'(r)$ functions, (3) the k_{max} values used to Fourier transform the measured $S(k)$ functions, the fitted r-space ranges for the $D'(r)$ functions, and the associated R_χ values, and (4) the fitted Si-O, Al-O, and Mg-O peak parameters for the $D'(r)$ functions.

[39] P. F. McMillan and R. J. Kirkpatrick, Am. Mineral. **77**, 898 (1992).

[40] M. J. Toplis, S. C. Kohn, M. E. Smith, and I. J. F. Poplett, Am. Mineral. **85**, 1556 (2000).

[41] S. Sasaki, K. Fujino, and Y. Takéuchi, Proc. Jpn. Acad., Ser. B **55**, 43 (1979).

[42] N. Morimoto and K. Koto, Z. Kristallogr. **129**, 65 (1969).

[43] P. B. Moore and J. V. Smith, Phys. Earth Planet. Inter. **3**, 166 (1970).

[44] H. Yang, R. M. Hazen, R. T. Downs, and L. W. Finger, Phys. Chem. Miner. **24**, 510 (1997).

[45] E. P. Meagher, Am. Mineral. **60**, 218 (1975).

[46] H. Xu, P. J. Heaney, P. Yu, and H. Xu, Am. Mineral. **100**, 2191 (2015).

[47] T. Yamanaka and Y. Takéuchi, Z. Kristallogr. **165**, 65 (1983).

[48] A. M. George and J. F. Stebbins, Am. Mineral. **83**, 1022 (1998).

[49] A. Pedone, G. Malavasi, M. C. Menziani, U. Segre, and A. N. Cormack, J. Phys. Chem. C **112**, 11034 (2008).

[50] M. Edén, Ann. Rep. NMR Spectr. **101**, 285 (2020).

[51] J. F. Stebbins, E. V. Dubinsky, K. Kanehashi, and K. E. Kelsey, Geochim. Cosmochim. Acta **72**, 910 (2008).

[52] L. M. Thompson and J. F. Stebbins, Am. Mineral. **96**, 841 (2011).

[53] L. M. Thompson and J. F. Stebbins, J. Non-Cryst. Solids **358**, 1783 (2012).

[54] Y. Ishii, M. Salanne, T. Charpentier, K. Shiraki, K. Kasahara, and N. Ohtori, J. Phys. Chem. C **120**, 24370 (2016).

[55] M. de Oliveira Jr., H. Damasceno, P. S. Salmon, and H. Eckert, J. Magn. Reson. Open **12-13**, 100067 (2022).

[56] R. A. Martin, P. S. Salmon, D. L. Carroll, M. E. Smith, and A. C. Hannon, J. Phys.: Condens. Matter **20**, 115204 (2008).

[57] N. E. Brese and M. O'Keeffe, Acta Crystallogr., Sect. B: Struct. Sci. **47**, 192 (1991).

[58] E. D. Lacy, Phys. Chem. Glasses **4**, 234 (1963).

[59] A. Jaworski, B. Stevensson, and M. Edén, J. Phys. Chem. C **120**, 13181 (2016).

[60] M. Guignard and L. Cormier, Chem. Geol. **256**, 111 (2008).

[61] E. Lorch, J. Phys. C: Solid State Phys. **2**, 229 (1969).

[62] J. R. Allwardt, S. K. Lee, and J. F. Stebbins, Am. Mineral. **88**, 949 (2003).

[63] P. Florian, A. Novikov, J. W. E. Drewitt, L. Hennet, V. Sarou-Kanian, D. Massiot, H. E. Fischer, and D. R. Neuville, Phys. Chem. Chem. Phys. **20**, 27865 (2018).

[64] A. Arora, D. B. Marshall, B. R. Lawn, and M. V. Swain, J. Non-Cryst. Solids **31**, 415 (1979).

[65] R. Brückner, J. Non-Cryst. Solids **5**, 123 (1970).

[66] R. D. Shannon, Acta Crystallogr. Sect. A **32**, 751 (1976).

[67] S. Sen, H. Maekawa, and G. N. Papatheodorou, J. Phys. Chem. B **113**, 15243 (2009).

[68] M. C. Davis, K. J. Sanders, P. J. Grandinetti, S. J. Gaudio, and S. Sen, J. Non-Cryst. Solids **357**, 2787 (2011).

[69] P. Zhang, P. J. Grandinetti, and J. F. Stebbins, J. Phys. Chem. B **101**, 4004 (1997).

[70] J. Schneider, V. R. Mastelaro, H. Panepucci, and E. D. Zanotto, J. Non-Cryst. Solids **273**, 8 (2000).

[71] D. C. Kaseman, A. Retsinas, A. G. Kalampounias, G. N. Papatheodorou, and S. Sen, J. Phys. Chem. B **119**, 8440 (2015).

[72] S. J. Watts, R. G. Hill, M. D. O'Donnell, and R. V. Law, J. Non-Cryst. Solids **356**, 517 (2010).

[73] D. R. Neuville and P. Richet, Geochim. Cosmochim. Acta **55**, 1011 (1991).

[74] D. R. Neuville and C. Le Losq, Rev. Mineral. Geochem. **87**, 105 (2022).

[75] N. K. Nasikas, T. G. Edwards, S. Sen, and G. N. Papatheodorou, J. Phys. Chem. B **116**, 2696 (2012).

[76] M. J. Toplis and D. B. Dingwell, Geochim. Cosmochim. Acta **68**, 5169 (2004).

[77] M. S. Aslanova, D. B. Dorzhiev, L. A. Sapozhkova, V. V. Gorbachev, A. S. Bystrikov, V. N. Petrakov, and V. I. Fertikov, Sov. J. Glass Phys. Chem. **8**, 26 (1982).

[78] *Handbook of Glass Properties*, edited by N. P. Bansal and R. H. Doremus (Academic Press, Orlando, 1986).

[79] B. Mysen and P. Richet, *Silicate Glasses and Melts*, Developments in Geochemistry 10 (Elsevier, Amsterdam, 2005), Chap. 8.

[80] P. S. Salmon and A. Zeidler, Structure and related properties of amorphous magnesium aluminosilicates, https://doi.org/10.15125/BATH-01139 (2022), University of Bath Research Data Archive.

[81] P. S. Salmon, B. G. Aitken, M. Buscemi, H. E. Fischer, L. V. D. Gammond, and A. Zeidler, Structure of magnesium aluminosilicate glass, https://doi.org/10.5291/ILL-DATA.6-05-988 (2018), Institut Laue-Langevin, Grenoble, France.

[82] P. S. Salmon, M. Buscemi, H. E. Fischer, L. V. D. Gammond, G. S. Moody, and A. Zeidler, Structure of GeS$_2$ glass by neutron diffraction with isotope substitution, https://doi.org/10.5291/ILL-DATA.6-05-976 (2018), Institut Laue-Langevin, Grenoble, France.

[83] P. S. Salmon, H. Eckert, H. E. Fischer, L. V. D. Gammond, R. Mendes Da Silva, H. Mohammadi, and A. Zeidler, Structural change in phosphate-based glassy precursors to superionic conducting glass-ceramic electrolytes, https://doi.org/10.5291/ILL-DATA.6-05-1009 (2019), Institut Laue-Langevin, Grenoble, France.

[84] P. S. Salmon, B. G. Aitken, H. E. Fischer, L. V. D. Gammond, R. Mendes Da Silva, H. Mohammadi, and A. Zeidler, Structure of magnesium aluminosilicate glass by neutron diffraction with isotope substitution, https://doi.org/10.5291/ILL-DATA.6-05-1002 (2019), Institut Laue-Langevin, Grenoble, France.

[85] E. Girón Lange, F. H. Cova, G. J. Cuello, H. Mohammadi, P. S. Salmon, G. Vaughan, and A. Zeidler, Structure of aluminosilicate glasses by NDIS, https://doi.org/10.5291/ILL-DATA.INTER-562 (2021), Institut Laue-Langevin, Grenoble, France.

[86] P. S. Salmon, M. Buscemi, C. Green, A. Hughes, A. C. Hannon, L. V. D. Gammond, and A. Zeidler, Structural role of magnesium in aluminosilicate glass, https://doi.org/10.5286/ISIS.E.RB1720342 (2017), STFC ISIS Neutron and Muon Source, UK.

[87] A. Zeidler, A. C. Hannon, B. G. Aitken, P. S. Salmon, L. V. D. Gammond, and R. Mendes Da Silva, Hardness anomaly in magnesium aluminosilicate (MAS) glass, https://doi.org/10.5286/ISIS.E.RB1820424 (2019), STFC ISIS Neutron and Muon Source, UK.